A&A, 709, A277 (2026)
https://doi.org/10.1051/0004-6361/202555848

Astronomy & Astrophysics

Large Interstellar Polarisation Survey

III. Observational constraints on the structure of grains

Ralf Siebenmorgen[1,⋆], Stefano Bagnulo[2], Lapo Fanciullo[3,4], Thomas Vannieuwenhuyse[1], and Vincent Guillet[5,6]

[1] European Southern Observatory, Karl-Schwarzschild-Str. 2, 85748 Garching, Germany
[2] Armagh Observatory and Planetarium, College Hill, Armagh BT61 9DG, UK
[3] National Chung Hsing University, 145 Xingda Rd., South Dist., Taichung City 402, Taiwan
[4] Tamkang University, 151 Yingzhuan Rd., Tamsui Dist., New Taipei City 251301, Taiwan
[5] Institut d'Astrophysique Spatiale, CNRS, Univ. Paris-Sud, Université Paris-Saclay, Bât. 121, 91405 Orsay cedex, France
[6] Laboratoire Univers et Particules de Montpellier, Université de Montpellier, CNRS/IN2P2, CC 72, Place Eugène Bataillon, 34095 Montpellier Cedex 5, France

Received 6 June 2025 / Accepted 30 March 2026

ABSTRACT

Our understanding of dust in the diffuse interstellar medium remains incomplete with regard to the structure, composition, size distribution, and alignment properties of its grains. Joint observations of reddening, starlight polarisation spectra, and polarised dust emission for individual sightlines provide essential constraints on such properties. We studied a far-UV-selected sample of 96 reddening curves, for which optical linear polarisation spectra were obtained with FORS at the VLT as part of the Large Interstellar Polarisation Survey. Starlight polarisation spectra for 60 stars are presented in this work. These data are combined with *Gaia* distance estimates and *Planck* thermal dust emission. A three-component dust model is made publicly available. It consists of nanoparticles, amorphous grains, and micrometre-sized dust agglomerates, with varying axial ratios, porosities, sizes, element abundances, and alignment efficiencies that match observations. The diversity of reddening and polarisation spectra is well reproduced by prolate grains with typical axial ratios of two, a porosity of 10%, and high alignment efficiencies. Such efficiencies can be achieved with radiative torque alignment theory but not with imperfect Davis–Greenstein alignment, except when adjusting the magnetic-field orientation to maximise the polarisation. Micrometre-sized dust contributes wavelength-independent grey extinction in the optical and accounts for about one-third of the visual extinction and one-third of the dust mass. A follow-up sub-millimetre survey with high-resolution polarimetry will further constrain grain shapes and alignment physics.

Key words. dust, extinction

1. Introduction

Dust is ubiquitous in the interstellar medium (ISM) and plays a significant role in many astrophysical processes. Clues as to the composition of interstellar dust come from various sources, such as observed elemental depletions in the gas phase and spectroscopic signatures of dust (Hensley & Draine 2021). The observed extinction curves display several spectral features, the most prominent being the 2175 Å bump, which is commonly attributed to graphite or polycyclic aromatic hydrocarbons (PAHs). Another important constraint is provided by dust emission, with conspicuous mid-IR emission bands often assigned to PAHs (Allamandola et al. 1989; Puget & Leger 1989). In addition, strong dust bands at 9.7 and 18 µm arise from the Si–O stretching and O–Si–O bending modes of silicate minerals, respectively (Dorschner et al. 1995). The extinction curve gives the dust extinction as a function of wavelength and provides strong constraints on dust models, in particular on the size distribution of the grains (Mathis et al. 1977).

The polarisation of starlight by dust extinction (Hall 1949; Hiltner 1949) and polarised thermal dust emission (Hildebrand 1988) show that interstellar dust grains are non-spherical and aligned with the interstellar magnetic field. This is the result of a rotating grain's axis of maximum inertia (**a**) aligning with its angular momentum (**J**; i.e. internal alignment) and **J** aligning with the magnetic-field-line direction (**B**; i.e. external alignment). Internal alignment is generally believed to be driven by the Barnett effect (Purcell 1979). Theories suggested to explain external alignment include paramagnetic relaxation (the Davis–Greenstein effect; Davis & Greenstein 1951) and the torque exerted by an anisotropic radiation field on a helical grain due to the differential scattering/absorption of left- and right-handed circular polarisation (radiative torque theory; Dolginov & Mitrofanov 1976; Draine & Weingartner 1996; Lazarian 1997).

In the imperfect Davis–Greenstein (IDG) alignment (Hong & Greenberg 1980; Voshchinnikov 2012) the grain wobbles and rotates around its axis of greatest momentum while also precessing around the magnetic field vector. A major criticism pointed out by Jones & Spitzer (1967) and Roberge & Lazarian (1999) is that the Davis–Greenstein (DG) model ignores internal alignment and therefore is a physically incorrect simplification.

Following the development of an analytical model for radiative alignment theories (RATs; Lazarian & Hoang 2007), and due to its good qualitative agreement with polarimetric observations (e.g. Andersson et al. 2015), interest in RATs has increased

⋆ Corresponding author: Ralf.Siebenmorgen@eso.org

significantly in the last two decades, and the original RAT has been significantly expanded. The high polarisation ceiling observed in dust thermal emission (~20%; Planck Collaboration XIX 2015a) requires that dust grains be more efficiently aligned than either the DG effect or the RAT alignment in its original form can account for. A solution found by Hoang & Lazarian (2016) is to consider grains with iron inclusions, which results in increased grain magnetic susceptibility and, therefore, alignment: this is called the magnetically enhanced RAT (MRAT). MRAT successfully accounts for grain alignment from the diffuse ISM to dense star-forming regions (Giang et al. 2025). Note that while DG torques are also increased by iron inclusions, they are typically significantly weaker than MRAT torques.

In this study we correlated observational constraints with the physical properties of interstellar dust. We tested a dust model against representative element depletions, stellar distance estimates, and the characteristics of reddening and polarisation in absorption and, where available, in emission, along individual sightlines through the diffuse ISM. Particular attention was paid to micrometre-sized dust agglomerates that absorb a fraction of the interstellar radiation field (ISRF; Mathis et al. 1983; Bianchi 2024). Because they are large, they remain cold and emit at long wavelengths. Initially, very cold (10 K) dust emission was detected in our Galaxy towards high-density regions (Chini et al. 1993) and in non-active galaxies (Chini et al. 1995). This cold dust was later confirmed by Infrared Space Observatory (Krügel et al. 1998; Siebenmorgen et al. 1999). More recently, excess emission at 0.5 mm observed by *Herschel* could not be explained by a single modified blackbody temperature component (Madden et al. 2013; Kennicutt et al. 2011; Rémy-Ruyer et al. 2013), with similar results confirmed using ALMA (Galliano et al. 2005) and LABOCA (Galametz et al. 2009) at even longer wavelengths. Furthermore, micrometre-sized particles originating from the local interstellar cloud surrounding the Solar System's ISM were directly measured in situ by the *Ulysses*, *Galileo*, and Stardust space probes (Landgraf et al. 2000; Westphal et al. 2014; Krüger et al. 2015). They appear in sightlines associated with the cold ISM (Siebenmorgen et al. 2020).

In the ISM, a grey component of micrometre-sized grains was introduced by Mathis et al. (1977) and Wang et al. (2015a,b) to account for the observed IR extinction. Such grains have also been incorporated into other dust models (Voshchinnikov 2004; Krügel & Siebenmorgen 1994; Krügel 2008; Ormel et al. 2011; Ysard et al. 2024). Recently, the impact of grey extinction on Type Ia supernova distance measurements was analysed by the Dark Energy Survey Collaboration (Popovic et al. 2024). The sub-millimetre excess continuum emission in the Milky Way detected by *Planck* (Planck Collaboration XII 2020) can be matched by adjusting the grain emissivity at these wavelengths (Hensley & Draine 2021). However, such models fail to resolve the discrepancy between trigonometric distance estimates provided by the Gaia Collaboration (2023) and the overprediction of the luminosity distance of the same stars (Siebenmorgen et al. 2025). Unification between luminosity and trigonometric distance estimates could be established by considering a population of micrometre-sized dust, which provides the necessary additional dimming of starlight. These grains are large enough to produce consistent reddening and grey extinction at wavelengths shorter than 1 μm.

For this purpose, the Large Interstellar Polarisation Survey (LIPS) was performed to measure the starlight polarisation spectra of 161 stars using the FORS instrument (Appenzeller et al. 1998) on the ESO Very Large Telescope (VLT). The observations covered a wavelength range of 0.38–0.95 μm at a spectral resolving power of ~880. In Paper I (Bagnulo et al. 2017), a catalogue of 127 linear polarisation spectra corresponding to 101 sightlines was published.

2. The sample and data

Observing sightlines that intersect different components of the ISM introduces complexities in relating extinction and polarisation data to physical dust parameters. To address this issue, in Paper II (Siebenmorgen et al. 2018) stars were observed with the high-resolution spectrograph UVES, which offers a resolving power of $\lambda/\Delta\lambda \sim 75\,000$ (Dekker et al. 2000; Smoker et al. 2009). These spectra were used to confirm the spectral type and luminosity class of the stars used for the reddening curve determination and to examine the profiles of interstellar absorption lines, particularly K I. The concept of 'single-cloud sightlines' was introduced, referring to cases where a dominant Doppler component accounts for more than half of the observed column density. A total of 65 such rare single-cloud sightlines were identified. It was found that interstellar polarisation is lower for multiple-cloud sightlines compared to single-cloud sightlines, indicating that the presence of additional clouds depolarises the transmitted radiation. Furthermore, significant variations in dust properties between different clouds were inferred from dust modelling.

In this work (Paper III), the sample is expanded with additional starlight polarisation spectra for 60 stars. The same observing strategy, data reduction, and calibration procedures as detailed in Paper I are applied (Bagnulo et al. 2017). Combining reddening and polarisation continuum observations is necessary to constrain the nature of interstellar dust, including its chemical composition and size distribution. For instance, the reddening rise in the far-UV is indicative of very small nanoparticles, and so is the 2175 Å bump (Stecher & Donn 1965; Blasberger et al. 2017), which is tied to carbonaceous nanoparticles. The shape of the polarisation curve in the optical (Serkowski et al. 1975) can be used to constrain the size distribution of aligned dust grains (Kim & Martin 1995; Vaillancourt et al. 2020).

The reddening curves have been derived in the near-IR (JHK) using the Two Micron All Sky Survey (2MASS; Cutri et al. 2003), in the optical (UBV) from ground-based facilities (Valencic et al. 2004), and in the far-UV below 0.3 μm down to the Lyman limit from space-based observations. At these short wavelengths, the International Ultraviolet Explorer (IUE) and the Far Ultraviolet Spectroscopic Explorer (FUSE) observed spectra for 417 stars (Valencic et al. 2004), 328 stars (Fitzpatrick & Massa 2007), and 75 stars with FUSE (Gordon et al. 2009). Furthermore, distances derived from *Gaia* parallaxes were used to estimate the reddening at infinite wavelength, providing an estimate of the visual extinction A_V (Siebenmorgen et al. (2025), Eq. (21)).

The LIPS sample is further complemented by observations of polarised dust emission obtained from the *Planck* observatory at 850 μm (Planck Collaboration XII 2020). The *Planck* total intensity and polarisation data were derived following the procedure outlined by Guillet et al. (2018) and colour corrected (Planck Collaboration XVII 2014b).

The available 0.09–2.3 μm reddening curves, complemented by UVES spectroscopy, *Planck* 850 μm (353 GHz) polarimetry, and 0.38–0.92 μm FORS spectropolarimetry, constitute the sample under investigation. It includes 96 stars, comprising 36 FORS polarisation spectra previously published in Paper I and Paper II, and 60 FORS polarisation spectra presented here. The

Table 1. Stars with derived *Planck*, reddening, FORS, and Serkowski parameters.

1	2	3	4	5	6	7	8	9	10	11	12	13	14	15	16	17
Star		*Planck*				Reddening				FORS				Serkowski		
Name	$\|\|b\|\|$	I_{850} MJy/sr	p_{850} %	θ_{850} °	A_V^{850} mag	A_V mag	$A_V^{\rm ref}$ mag	Ref	SM	Date	p_V %	θ_V °	$\mathrm{d}\theta/\mathrm{d}\lambda$ °/µm	$p_{\max}$ %	$\lambda_{\max}$ µm	$k_{\rm pol}$
HD 024263	35	1.00	6.0± 2.4	77± 18	0.8	–	0.7	V	S	2019-02-24	1.1 ± 0.1	149 ± 0.5	2 ± 0.7	1.08	0.58	1.04
…																
Walker 67	1	58.9	1.1± 2.3	91± 16	49	–	0.7	F	S	B17	4.1 ± 0.3	17 ± 0.6	–6 ± 1.2	5.17	0.81	1.47

Notes. The entries for all 96 stars are provided in Table A.1. The columns are explained in Sect. 2. B17 stands for Bagnulo et al. (2017), and S14 for Siebenmorgen et al. (2014).

characteristics of the sample are summarised in Table 1, which lists the following 17 columns: for each star (Col. 1), we specify the absolute Galactic latitude $|b|$ (Col. 2). The *Planck* results are presented in four columns: surface brightness (I_{850} in MJy/sr) in Col. 3, fractional polarisation (p_{850} in %) in Col. 4, the polarisation angle in equatorial coordinates (θ_{850} in °) in Col. 5, and an estimate of the visual extinction A_V^{850} (Col. 6), which is based on the *Planck* map of the dust optical depth at 850 µm (Planck Collaboration XXI 2015b).

The visual extinction ($A_{\rm V}$) as determined from the *Gaia* parallax (π; Col. 7) and the reference extinction ($A_{\rm V}^{\rm ref}$; Col. 8) are provided. The latter was estimated by extrapolating optical/near-IR reddening to an infinite wavelength, as given in the reddening curve catalogues by Valencic et al. (2004, labelled 'V'), Fitzpatrick & Massa (2007, labelled 'F'), and Gordon et al. (2009, labelled 'G') in Col. 9. We classified 55 as single-cloud sightlines (labelled 'S') and 41 as multi-cloud sightlines (labelled 'M'; Col. 10).

The results of the FORS spectropolarimetry are summarised across seven columns. Observing dates are listed in Col. 11. For stars observed multiple times, the final polarisation spectra are derived by averaging the Stokes parameters from individual observations. The fractional polarisation ($p_{\rm V}$) and polarisation angle in equatorial coordinates ($\theta_{\rm V}$) at 0.55 µm are provided in Cols. 12–13. The gradient in the polarisation angle along the spectrum, $\mathrm{d}\theta/\mathrm{d}\lambda$ (°/µm) is given in Col. 14. In the optical, the observed interstellar polarisation spectra can be well approximated by a mathematical expression known as the Serkowski formula:

$$p(\lambda) = p_{\max}\ \exp\left[-k_{\rm pol}\ \ln^2\left(\frac{\lambda_{\max}}{\lambda}\right)\right], \qquad (1)$$

The Serkowski et al. (1975) parameters ($p_{\max}$, $\lambda_{\max}$, and $k_{\rm pol}$) derived from spectral fits to the FORS polarisation spectra are provided in Cols. 15–17. The Serkowski fits for 43 stars, for which the available data do not permit detailed dust modelling, are shown in Fig. A.1. The spectral variation of the FORS polarisation angle, corrected for the optical reference value ($\theta - \theta_V$) is shown in Fig. A.2.

In the LIPS sample, 27 stars are included in the stellar polarisation catalogue of Heiles (2000), who detected 19 of these stars with high confidence at $p \gtrsim 0.6\%$. For these 19 stars, the linear polarisations in the two catalogues are in agreement, at $|p_{\rm FORS} - p_{\rm Heiles}| = 0.14 \pm 0.08\%$. The polarisation angles are consistent within 3°, except for HD 092044, where the polarisation angles differ by 18°.

3. Dust model

We applied the dust model from Siebenmorgen (2023), which is consistent with current observational constraints on dust in the diffuse ISM (Hensley & Draine 2021). The model adopts representative solid-phase elemental abundances and successfully reproduces the observed wavelength-dependent reddening, emission, and polarisation from interstellar dust, spanning from the UV to microwave wavelengths. Furthermore, the model includes grey extinction by micron-sized grains, which reduces the luminosity distance, enabling consistency with trigonometric distances derived from *Gaia* parallaxes.

3.1. Grain composition and size distributions

The number densities of grains follow a power-law size distribution, $n(r) \propto r^{-q}$, where r is the grain radius, and q the power-law exponent assumed to be the same for each of the three dust components:

(i) Nanoparticles ($r \lesssim 6$ nm), including very small silicate (vSi), very small graphite (vgr), and PAHs.

(ii) Amorphous grains of silicate (aSi) and carbon (aC; 6 nm $\lesssim$ r $\lesssim$ 250 nm). These grains are considered to have prolate shapes (rather than oblate) since they provide a better fit to observed linear polarisation spectra (Siebenmorgen et al. 2014). The mean radius of the amorphous grains, averaged over the size distribution, is typically $\bar{r}_{\rm aC,aSi} \sim 30$ nm.

(iii) Micrometre-sized dust agglomerates (250 nm $\lesssim$ r < 3 µm) are treated as porous composites of amorphous silicate and carbon grains The mean radius of these micrometre-sized prolate shaped grains remains below 1 µm. We denote with r_i^- and r_i^+ the low and upper limit of grain sizes for population i, respectively. The radius of spheroids is defined as that of a sphere of the same volume ($r^3 = ab^2$), where a is the grain major axis and b its minor axis.

Optical constants are adopted from Zubko et al. (1996) for amorphous carbon, Draine (2003) and Draine & Hensley (2021) for graphite and astro-silicate, and Demyk et al. (2022) for amorphous silicates, assuming a 97:3 mix in mass of MgO–0.5 SiO_2 and $Mg_{0.8}Fe^{2+}_{0.2}$ SiO_3. The optical constants of porous and composite grains with vacuum inclusions are computed using the Bruggemann mixing rule. The molecular weights are $\mu_{\rm C} = 12$ for carbon materials, $\mu_{\rm Si} = 135$ for astro-silicate, and $\mu_{\rm aSi} = 100$ for amorphous silicates. The bulk densities (g/cm^3) are for nanoparticles $\rho_{\rm vgr} = 2.2$, $\rho_{\rm vSi} = 3.5$, carbon particles $\rho_{\rm aC} = 1.6$, amorphous silicates $\rho_{\rm aSi} = 2.7$, and in micrometre-sized grains $\rho_{\mu\rm Si} = 3.4$.

3.2. Grain alignment

Draine & Fraisse (2009) introduced an alignment function where $f_{\rm align} = 0$ represents random orientation and $f_{\rm align} = 1$ corresponds to perfect spinning alignment. The alignment function, $f_{\rm align}(r)$, is strongly size-dependent: $f_{\rm align} = 0$ for $r \lesssim 50$ nm, then increases for larger grains, reaching its maximal value

for $r_{\rm pol}^{-} \sim 100\,$nm, remaining constant for larger grains. This modelling is consistent with the size-dependence of alignment efficiency observed for the individual sightlines analysed in Paper II (Siebenmorgen et al. 2018): the starlight polarisation spectra are well reproduced when only large particles, at $r \gtrsim r_{\rm pol}^{-}$, are aligned, while smaller particles remain unaligned.

Radiative torques can align the angular momentum vector (**J**) of the grains with the magnetic field (**B**) in two distinct regimes characterised along the high-**J** and low-**J** attractor points. The high-**J** attractor corresponds to perfect alignment and applies to materials with ferromagnetic inclusions. The low-**J** point is less well constrained, and so is the fraction of high-**J** to low-**J** attractors, which is of interest when applied to paramagnetic materials. We applied a simplified RAT alignment model similar to Reissl et al. (2020), with alignment efficiency

$$\tilde{f}_{\rm align}(r) = \begin{cases} f_{\rm align} & : r_{\rm pol}^{-} \lesssim r \lesssim r_{\rm des}\,, \\ 0 & : \text{otherwise.} \end{cases} \quad (2)$$

Grains below a minimum alignment radius $r_{\rm pol}^{-}$ are randomly oriented. Supra-thermally rotating particles with radius above $r_{\rm des} \sim 1\,\mu$m disrupt because of the centrifugal stress (Hoang et al. 2021). The destruction radius depends on material properties of the grains, such as tensile strength, composition, and structure, as well as on environmental parameters, including intensity, hardness, and anisotropy of the ISRF. Such large grains do not contribute to the optical polarisation. For simplicity, we set $r_{\rm des}$ to the maximum grain radius. Only grains with radii $r_{\rm pol}^{-} \lesssim r \lesssim r_{\rm des}$ are aligned at constant efficiency $f_{\rm align}$, where we neglect a mild size dependence of the fraction of low-J attractors (Hoang & Truong 2024).

3.3. Computing grain cross-sections over grain dynamics

Figure 1 presents the geometry of the problem for a prolate grain with a spinning axis perfectly aligned with the magnetic field. The plane of the sky is the xy-plane. The sightline is along the z axis and light coming towards us (**k**). The magnetic field **B** lies in the (yz) plane. The magnetic field angle Ω is measured from the sightline z towards **B**. Maximum polarisation is observed for $\Omega = 90°$ and no polarisation for $\Omega = 0°$. The spinning plane of the grain is perpendicular to **B**, with φ the spin angle of the grain symmetry axis **a** with respect to the x axis. To compute the grain extinction and polarisation cross-sections, we considered a linearly polarised electromagnetic wavevector ($\boldsymbol{k}$). The plane of incidence is the plane containing **k** and **a**. We denote with α the angle between **a** and **k**, whose sector is contained in the plane of incidence. We also define Φ as the angle between the x axis and the projection of **a** onto the plane of the sky. The angles α and φ are related to Ω and Φ as

$$\cos\alpha = \sin\Omega\cos\varphi\,, \quad (3)$$

$$\tan\Phi = \cos\Omega\tan\varphi\,. \quad (4)$$

For symmetry reasons, for the calculations one only needs to consider values for Ω and φ between 0 and $\pi/2$, resulting in values for α and Φ also between 0 and $\pi/2$. The polarisation cross-section, integrated over the spinning angle (φ), is (focusing here on the dependence on angles and radius only)

$$C_{\rm pol}(\Omega, r) = 2\, f_{\rm align}\, r^2 \int_0^{\pi/2} (Q_{\rm ext}^{\rm TM}(\alpha, r) - Q_{\rm ext}^{\rm TE}(\alpha, r)) \cos 2\Phi \,{\rm d}\varphi\,, \quad (5)$$

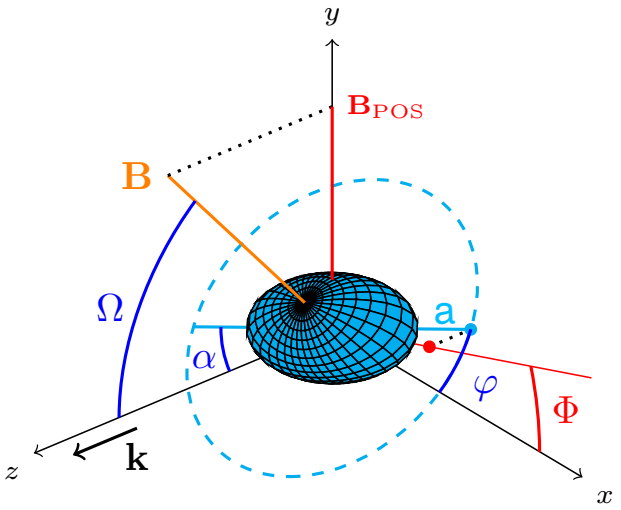

Fig. 1. Geometry of a perfectly aligned spinning prolate particle with long-side symmetry axis **a**. The sky is in the xy plane. The angle Φ (red) is between the x axis and the projection of **a** onto the plane of the sky. The sightline is the z axis, with electromagnetic wavevector ($\boldsymbol{k}$) approaching us. The magnetic field (**B**) lies in the yz plane with the magnetic field angle (Ω) measured from z towards **B**. The grain spinning plane is perpendicular to **B** (dashed blue circle) and includes **a**. The grain spinning angle (φ; blue) is measured on the x axis. The angle of incidence (α) is given between **a** and **k**. Note the relation between Ω, α, and φ as given in Eq. (3).

where $Q_{\rm ext}^{\rm TE}$ (resp. $Q_{\rm ext}^{\rm TM}$) is the transverse electric (respectively transverse magnetic) grain extinction cross-section computed for an electromagnetic wave of wavevector $\boldsymbol{k}$ with an oscillating electric field vector, $\boldsymbol{E}$ (respectively oscillating magnetic field vector, $\boldsymbol{H}$) perpendicular to the plane of incidence as defined by Bohren & Huffman (1983). The efficiency factors $Q(\lambda, r, a/b, m, \alpha)$ depend on the wavelength (λ), the grain radius (r), the axial ratio (a/b), the optical constants (m), and the angle of incidence (α), which in turn depends on the given alignment model of the magnetic field angle, Ω (Eq. (3)). Computation of the efficiency factors for large spheroids becomes difficult. They are computed using Voshchinnikov & Farafonov (1993) and custom software provided by Voshchinnikov (2004). The code converges for size parameters $x = 2\pi a/\lambda$ up to $|m-1|\,x \sim 22$. At such or even larger values of x, we replaced the extinction cross-section of the spheroids with that of spheres using Mie theory and set the polarisation $Q_{\rm pol}(\lambda) = 0$. At $x > 22$, such large grains do not contribute significantly to the observed starlight polarisation in the optical. The absorption and scattering cross-sections for aligned particles is

$$C_{\rm abs,sca}^{\rm align}(\Omega, r) = 4\, f_{\rm align}\, r^2 \int_0^{\pi/2} (Q_{\rm abs,sca}^{\rm TM}(\alpha, r) + Q_{\rm abs,sca}^{\rm TE}(\alpha, r)) \cos 2\Phi \,{\rm d}\varphi\,. \quad (6)$$

For randomly aligned grains, $C_{\rm abs,sca}^{\rm rand}$, we applied Eq. (3.34) from Voshchinnikov (2012). The grain absorption and scattering cross-sections are

$$C_{\rm abs,sca}(\Omega, r) = \tilde{f}_{\rm align}(r)\, C_{\rm abs,sca}^{\rm align}(\Omega, r) + \left(1 - \tilde{f}_{\rm align}(r)\right) C_{\rm abs,sca}^{\rm rand}(r)\,, \quad (7)$$

and $C_{\rm ext} = C_{\rm abs} + C_{\rm sca}$ is the grain extinction cross-section (cm^2).

3.4. Cross-sections per unit mass of dust

The total absorption, scattering, or polarisation cross-section $K_i(\lambda)$ per unit mass (cm^2/g-dust) for dust component i is

$$K_i(\lambda) = \frac{3}{4\pi}\,\frac{m_i}{\rho_i}\,\frac{\int_{r_i^-}^{r_i^+} C_i(r,\lambda)\, r^{-q}\,\mathrm{d}r}{\int_{r_i^-}^{r_i^+} r^{3-q}\,\mathrm{d}r}\,, \tag{8}$$

where $C_i(r,\lambda)$ is the corresponding absorption, scattering, or polarisation cross-section for a grain of radius r at wavelength λ (Eqs. (5)–(7)), ρ_i is the bulk density for population i, and m_i is the mass of component i per unit mass of dust:

$$m_\mathrm{i} = \mu_\mathrm{i}\,\frac{[\mathrm{X_i}]}{[\mathrm{H}]}\Big/\sum_i \mu_\mathrm{i}\,\frac{[\mathrm{X_i}]}{[\mathrm{H}]}. \tag{9}$$

The elemental abundance in the dust relative to hydrogen in the gas phase $[\mathrm{X_i}]/[\mathrm{H}]$ is constrained to respect the depletion limits (Hensley & Draine 2021; Siebenmorgen 2023) so that

$$\frac{[\mathrm{C}]}{[\mathrm{Si}]} < 5.2. \tag{10}$$

The total dust cross-section, $K(\lambda)$, is the sum of K_i from all components[1].

3.5. Dust observables in extinction

The optical depth $\tau_V = A_V/1.086$ is

$$\tau_V = N^\mathrm{na}\,K_V^\mathrm{na} + N^{\mu\mathrm{A}}\,K_V^{\mu\mathrm{A}}, \tag{11}$$

where N^na represents the sum of the dust column density of nanoparticles and amorphous particles, while $N^{\mu\mathrm{A}}$ is the dust column density of micrometre-sized grains. The corresponding mass extinction cross-sections are denoted by K_V^na and $K_V^{\mu\mathrm{A}}$, respectively. At infinite wavelengths, $K(\infty) = 0$, so $A_V = -E(\infty - V) > -E(H - V)$ in the H band. The reddening $E(B-V) = 1.086\,(\tau_B - \tau_V)$ is expressed (with our notations) as

$$E(B-V) = N^\mathrm{na}\,(K_B^\mathrm{na} - K_V^\mathrm{na}) + N^{\mu\mathrm{A}}\,(K_B^{\mu\mathrm{A}} - K_V^{\mu\mathrm{A}}), \tag{12}$$

providing a second constraint for estimating the relative mass fraction of the micrometre-sized grains, $m_{\mu\mathrm{A}} = N^{\mu\mathrm{A}}/(N^n + N^{\mu\mathrm{A}})$. From this we derived the absolute reddening of the model,

$$E(\lambda - V) = \frac{2.5}{\ln 10}\,(\tau_\lambda - \tau_V)\,, \tag{13}$$

and the starlight polarisation spectrum,

$$p(\lambda) = N\,K_\mathrm{pol}(\lambda), \tag{14}$$

where $N = N^\mathrm{na} + N^{\mu\mathrm{A}}$ (g-dust/cm^2) is the total dust column density and K_pol (cm^2/g-dust) the total linear polarisation cross-section (Eq. (8)).

The dust model accounts for representative solid-phase element abundances of the main absorbing dust components of the assumed grain stoichiometry and explains phenomena such as wavelength-dependent reddening, starlight polarisation, and the emission of unpolarised and polarised light. It also provides the necessary grey extinction for reconciling the luminosity distances with the *Gaia* parallaxes (Siebenmorgen et al. 2025). We compared it with the LIPS sample.

[1] A suffix or index 'abs' indicates absorption, 'ext' extinction, 'pol' polarisation, 'sca' scattering, 'des' destruction, 'tot' total, and 'μA' micrometre-sized agglomerates.

3.6. Infrared emission per gram of dust

The emissivity, $\epsilon_i(r)$, per gram of dust for a grain of population i and particle radius r was determined from the energy balance between emission and absorption of photons from the mean intensity $J^\mathrm{ISRF}(\lambda)$ of the ISRF (Mathis et al. 1983):

$$\int K_{abs,i}(\lambda, r)\,J^\mathrm{ISRF}(\lambda)\,\mathrm{d}\lambda = \int K_{abs,i}(\lambda, r)\,P(T)\,B_\lambda(T)\,\mathrm{d}T\,\mathrm{d}\lambda\,, \tag{15}$$

where $\epsilon_i(r)$ is given by the right-hand side, T refers to the temperature of material i and particle radius r, $B_\lambda(T)$ is the Planck function, and $P(T)$ is the temperature distribution function (Guhathakurta & Draine 1989; Krügel 2008). This function is evaluated using an iterative scheme by Siebenmorgen et al. (1992). Quantum heating of the dust, and thus $P(T)$, needs to be evaluated only for nanoparticles, as $P(T)$ approaches a δ-function for the larger amorphous and micrometre-sized grains. The total emissivity, ϵ, is the sum of the emissivity from all dust components.

The total polarised emission ($\epsilon_\mathrm{i,pol}$) of population i was computed by summing the contributions from the minimum alignment radius ($r_\mathrm{i,pol}^-$) to the maximum radius (r_i^+):

$$\epsilon_\mathrm{i,pol}(\lambda, r) = f_\mathrm{align}\int_{r_\mathrm{i,pol}^-}^{r_\mathrm{i}^+} K_\mathrm{i,pol}(\lambda, r)\,B_\lambda(T)\,\mathrm{d}r, \tag{16}$$

where $K_\mathrm{i,pol}$ is given by Eq. (8), and T refers to the temperature of material i and particle radius r. The total polarised dust emission, ϵ_pol, is the sum of the polarised emission from all components contributing to the polarisation, which include the amorphous and the micrometre-sized grains. The corresponding fractional polarisation from dust emission is

$$p = \frac{\epsilon_\mathrm{pol}}{\epsilon}. \tag{17}$$

3.7. Infrared emission per H atom

More material along a given sightline will increase both $E(B-V)$ and N_H. Observationally, it is assumed that the reddening scales approximately linearly with the dust column density and, if well mixed, also with the hydrogen column density such that $N_\mathrm{H}/E(B-V)$ remains roughly constant. Bohlin et al. (1978) derived $N_\mathrm{H}/E(B-V) = 5.8$ (with this value and subsequent values given in 10^{21}H-atoms cm^{-2} mag^{-1}), which is close to the value of 5.9 found for translucent clouds (Rachford et al. 2009). However, significantly different values have been reported: 4.9 (Diplas & Savage 1994), 7.5 (Ensor et al. 2017), 9.4 (Nguyen et al. 2018), $N_\mathrm{HI}/E(B-V) = 8.3$ (Liszt 2014), and 8.8 (Lenz et al. 2017). These differences are consistent with systematic variations in the gas-to-dust mass ratio, with lower values in the Galactic plane and higher values at high Galactic latitudes.

The total dust mass, M_dust, was estimated by summing all atoms depleted from the gas phase and scaling by the molecular weights corresponding to the assumed grain stoichiometry. The gas mass, $M_\mathrm{gas} \sim 1.4\,M_\mathrm{H}$, was calculated by summing the contributions of helium and hydrogen, assuming a He:H ratio of 1:10. At high Galactic latitudes, the derived gas-to-dust mass ratio ($M_\mathrm{gas}/M_\mathrm{dust}$) is ~125 (Hensley & Draine 2021; Siebenmorgen 2023). This ratio can vary by up to ~50% while still being consistent with elemental depletion. However, because we use relative dust abundances in our dust model, such variations, if

applied to all components (Eq. (9)), do not affect the fit to the reddening curves.

The gas-to-dust mass ratio and the hydrogen column density are used to scale the dust emission in the model ϵ (Eq. (15)) in erg s^{-1} Hz^{-1} sr^{-1} per g-dust to the *Planck* surface brightness I (erg s^{-1} Hz^{-1} sr^{-1} cm^{-2} per H-atom) at 353 GHz, with atomic mass unit m_u:

$$N_{\rm H} = \frac{1}{m_u} \frac{M_{\rm gas}}{M_{\rm dust}} \frac{I}{\epsilon}. \tag{18}$$

For our nominal dust composition (Sect. 4.1), we find that the $N_{\rm H}/E(B-V)$ ratio is 6.3 for HD 027778, 7.6 for HD 108927, and 7.3 for HD 287150, in units of 10^{21} H-atoms cm^{-2} mag^{-1}. These values are consistent with the reference values and fall within the uncertainty range of the gas-to-dust mass ratio ($M_{\rm gas}/M_{\rm dust}$).

3.8. Dust model fitting procedure

The dust model is applied to sightlines with available high-quality far-UV selected reddening curves, visual extinction values derived from *Gaia* distance estimates (A_V; Eq. (21)), near-IR reddening using 2MASS, starlight polarisation spectra obtained with FORS, and the colour-corrected (Planck Collaboration XVII 2014b) total and polarised emission observed by *Planck*. Best-fit dust parameters are derived using a three-step iterative procedure, under the assumption that along a given sightline where dust extinction dominates, the magnetic-field direction does not vary significantly. For sightlines where the optical polarisation spectrum does not follow the Serkowski curve (Sect. 4.3), the inferred magnetic-field direction should be regarded with caution.

Initially, the reddening curve is fitted using the publicly available χ^2 minimisation tool `absredgaia` (Siebenmorgen 2025). This tool returns the χ^2_r of the best fit to the reddening curve and the seven model parameters: the exponent of the size distribution (q) and the relative mass fractions of the different dust components: $m_{\rm vgr}$, $m_{\rm vSi}$, $m_{\rm PAH}$, $m_{\rm aC}$, $m_{\rm aSi}$, and $m_{\mu\rm A}$. These relative dust masses are linked to the element abundances (Eq. (9)). The tool adheres to the depletion limits set by Eq. (10). Dust parameters of the general field of the ISM (Siebenmorgen 2023) are chosen as starting parameters, with an upper radius $r^+_{\mu\rm A} = 3$ µm.

In the second step, the starlight polarisation spectrum is fitted by varying the minimum alignment radii of the amorphous carbon and silicate grains, $r^-_{\rm pol,\,aC}$ and $r^-_{\rm pol,\,aSi}$, together with the magnetic-field orientation, using $\Omega = 45°$ as the initial value. The polarisation spectra of the dust model $p(\Omega, r^-_{\rm pol,\,aC}, r^-_{\rm pol,\,aSi}, \lambda)$ were compared with the FORS data, and the corresponding $\chi^2_{\rm pol}$ values were computed. The grain radii in the model grid increase by 5% from one bin to the next. The dust model was evaluated for 40×40 pairs of $r^-_{\rm pol,i}$ with $i \in \{\rm aC, aSi\}$ in the range 50–250 nm. The values of $r^-_{\rm pol,\,aC}$ and $r^-_{\rm pol,\,aSi}$ that best match the shape of the observed polarisation spectra are identified. Next, the magnetic-field orientation (Ω) was varied and $C_{\rm pol}(\Omega, r)$ (Eq. (5)) computed. The model that best reproduces the Serkowski maximum (p_V; Col. 15 of Table 1) was selected. For this value of Ω, a new set of $r^-_{\rm pol,\,aC}$ and $r^-_{\rm pol,\,aSi}$ was derived. The best-fitting parameters ($r^-_{\rm pol,\,aC}$, $r^-_{\rm pol,\,aSi}$, and Ω) were extracted from the model that minimises $\chi^2_{\rm pol}$. Because the extinction cross-section depends on the magnetic-field orientation (Eq. (7)), both steps – fitting the reddening and fitting the polarisation spectra – were iterated.

Planck Collaboration XII (2020) introduced two criteria for constraining dust models by examining the ratio of sub-millimetre-to-optical polarisation. These are the ratio of the fractional polarisation at 850 µm to the optical polarisation efficiency and the ratio of the polarised emission intensity $P_{850} = p_{850}\, I_{850}$ (MJy/sr) to the optical polarisation,

$$R_{\rm S/V} = p_{850}/(p_V/\tau_V)\,, \tag{19}$$

$$R_{\rm P/p} = P_{850}/p_V\,. \tag{20}$$

In the third step, the best-fit parameters from step 2 were retained, and the upper grain radius was varied within the range $0.25 < r^+_{\mu\rm A} \lesssim 3$ µm. This resulted in 50 models for which the *Planck*-to-FORS polarisation ratios $R_{\rm S/V}$ and $R_{\rm P/p}$, along with their corresponding goodness-of-fit parameters χ^2_r, $\chi^2_{\rm pol}$, $\chi^2_{R_{\rm S/V}}$, and $\chi^2_{R_{\rm P/p}}$, were computed. These χ^2 values were normalised to their respective median. We then derived the total goodness-of-fit parameter by assigning equal weight to the reddening curve, the optical polarisation spectrum, and the *Planck* ratios: $\chi^2_{\rm tot}$. The upper radius of the micrometre-sized dust ($r^+_{\mu\rm A}$) corresponds to the minimum of $\chi^2_{\rm tot}(r^+_{\mu\rm A})$. Steps 1–3 were iterated to determine the final set of ten model parameters (Cols. 4–13 in Table 2) for a given axial ratio (a/b) and porosity ($V_{\rm Vac}$) of the grains. The upper grain radius is typically $r^+_{\mu\rm A} = 1$ µm, and we identify it with the destruction radius $r_{\rm des} = r^+_{\mu\rm A}$ in Eq. (2). Even larger, non-aligned grains could potentially exist, but they would not, or only marginally, contribute to the observations.

The polarised emission spectrum is shown for three sightlines in Fig. 2. At 850 µm, the polarisation is dominated by the micrometre-sized dust particles. By increasing the radius $r^+_{\mu\rm A}$, these grains become cooler, and their polarisation spectrum shifts to longer wavelengths, so that the polarised intensity P_{850} increases as long as one remains in the Rayleigh part of the spectrum of the micrometre-sized dust. On the other hand, by decreasing $r^+_{\mu\rm A}$, the micrometre-sized agglomerates approach temperatures of the amorphous components, causing the polarisation spectra of the two components to merge.

In the optical range, the micrometre-sized dust provides a grey (constant) reddening and has a marginal impact on the best-fitting model parameters, whereas in the near-IR, the reddening of sightlines with a significant amount of micrometre-sized grains is strongly impacted by $r^+_{\mu\rm A}$. Therefore, varying $r^+_{\mu\rm A}$ will change the fitting parameters of the reddening curve, necessitating repetition of the procedure. Fortunately, in the three steps, the dependences on the free model parameters are weak and converge after one to two iterations. The FORS and *Planck* data are fitted without considering polarisation by nanoparticles ($r < r^-_{\rm pol}$).

4. Observational constraints on grain structure and alignment efficiency

Observations of dust polarisation in both absorption and emission provide complementary, in principle orthogonal, perspectives on dust grains, allowing constraints to be placed on their shapes, porosity, and alignment efficiencies.

4.1. Pristine sightlines

A high-quality sample of far-UV selected reddening curves was derived by Siebenmorgen et al. (2023). Stars with multiple bright

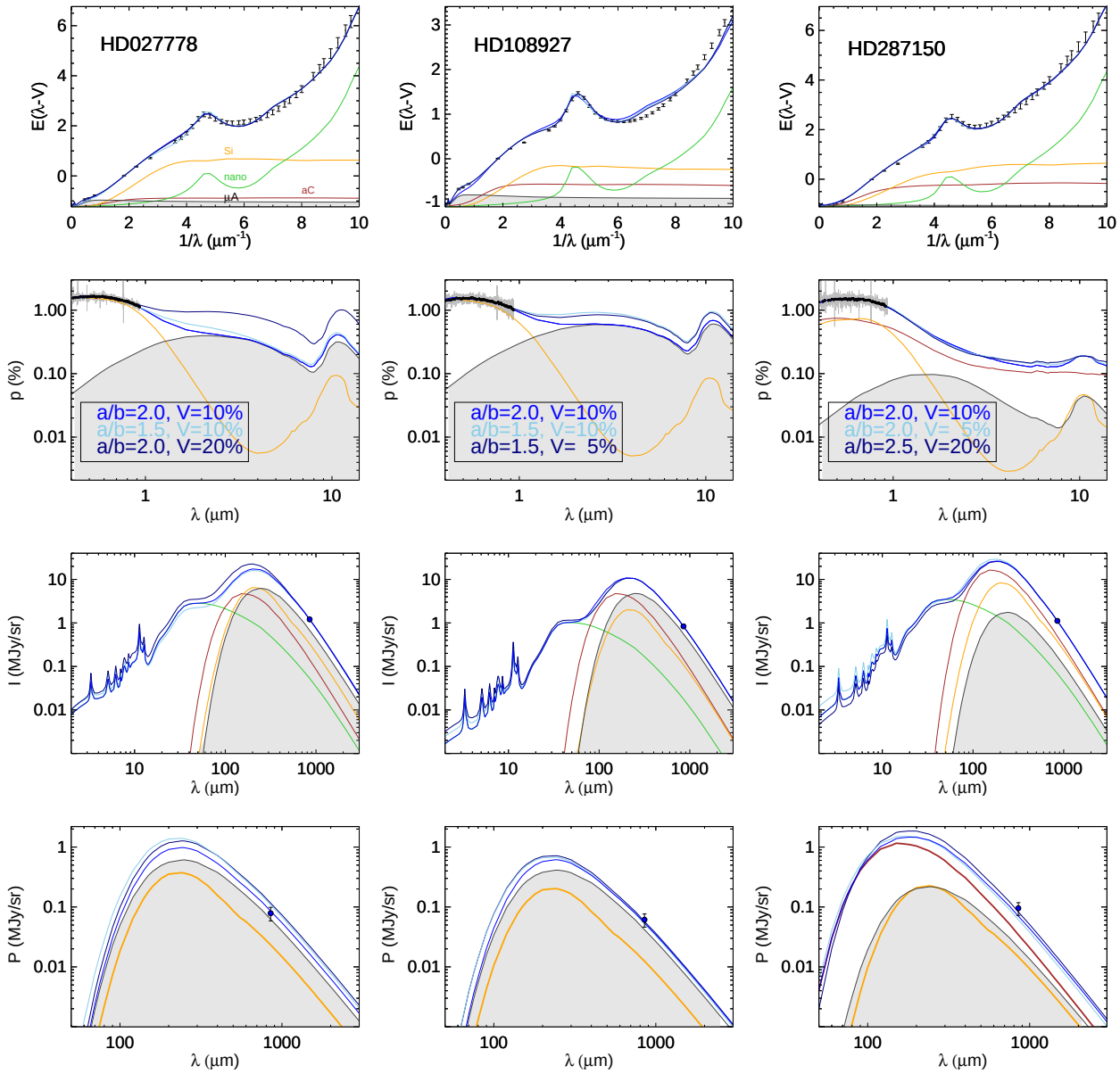

Fig. 2. Dust models for HD 027778 (left), HD 108927 (middle), and HD 287150 (right). For each sightline we show, from top to bottom, the reddening curve, the optical polarisation spectrum, and the total and polarised (I and P) dust-emission spectrum. The reddening-curve data with error bars are described in the text. The observed starlight polarisation is shown for the unbinned spectrum (grey lines) and for data binned to a spectral resolution of $\lambda/\Delta\lambda \sim 50$ (black circles). The dust emission is consistent with *Planck* 353 GHz measurements (filled circles). Model curves with the adopted a/b ratio and porosity (V) are indicated in the legend. The individual contributions to the observables are shown for nanoparticles (green), amorphous carbon grains (brown), silicates (orange), and micrometre-sized agglomerates (grey shading) for the best-fit model with the parameters listed in Table 2.

objects in the IUE (Valencic et al. 2004; Fitzpatrick & Massa 2007) and FUSE (Gordon et al. 2009) apertures were excluded. Only stars for which the spectral type and luminosity class, as derived from UVES high-resolution spectroscopy, confirm those used in the reddening estimation were retained. Furthermore, the photometric variability of stars in the high-quality sample, in both the V and G bands, and in the $B-V$ colour, was restricted to $\lesssim$0.03 mag.

The visual extinction A_V (Table A.1) was derived following Siebenmorgen et al. (2025) by inserting the absolute magnitude M_V and *Gaia* distance estimates D_{Gaia} into the photometric equation:

$$A_V = V - M_V - 5\log D_{Gaia} + 5. \quad (21)$$

The absolute magnitude (M_V) was extracted from the catalogues of Bowen et al. (2008) and Wegner (2006) for the spectral type and luminosity class provided by Siebenmorgen et al. (2023). The distances were estimated using *Gaia* Data Release 3 (DR3; Gaia Collaboration 2023). To ensure a reliable astrometric solution, only stars with a re-normalised unit weight error below 1.2 were included (Luri et al. 2018). In addition, the G-magnitude-dependent parallax error $\sigma(\pi, G)$ was computed following Maíz Apellániz (2022), and only stars with a parallax precision of $\pi/\sigma(\pi, G) > 10$ were considered. The simple inverse of the DR3 catalogue parallax typically agrees with $D_{\rm Gaia}$ within 2%. Since parallactic distances inherently depend on priors, we verified that our distance estimate $D_{\rm Gaia}$ aligns with other probabilistic distance estimates within 1–2% (Bailer-Jones et al. 2021).

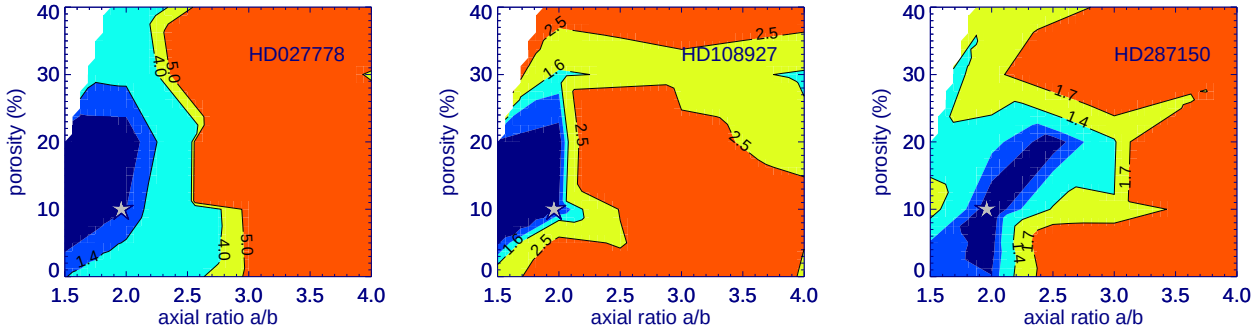

Fig. 3. Total goodness-of-fit ($\chi^2_{\rm tot}$), normalised to the nominal model (grey symbol), as a function of axial ratio a/b and porosity for HD 027778 (left), HD 108927 (middle), and HD 287150 (right). Regions with successful fits at $\chi^2_{\rm tot} \lesssim 1$ are shown in blue.

Three stars exhibiting H-band extinction greater than their visual extinction A_V were removed from the subsample, as their luminosity distance is smaller than the trigonometric distance. These selection criteria result in a pristine sample of 27 sightlines that are suitable for dust modelling.

Extinction probes the ISM in the foreground of the star, while emission traces the entire sightline. Planck Collaboration XXI (2015b) established selection criteria for sightlines in order to obtain polarisation measurements of the same dust grains at different wavelengths. For this purpose, the visual extinction derived from the star's reddening must be comparable to the visual extinction estimated from the *Planck* maps. This criterion excludes sightlines with significant dust emission originating from material located behind the star. The limited 40′ resolution of the *Planck* polarisation maps prevents a direct comparison with starlight polarisation measurements of individual stars at low Galactic latitudes. However, at Galactic latitudes $|b| \gtrsim 15°$, three stars HD 027778, HD 108927, and HD 287150 exhibit significant starlight and *Planck* polarisation with comparable extinction values, $A_V^{850} \sim A_V$ (Table A.1). In addition, these stars show the expected reversal in polarisation angle between the polarised emission and the starlight polarisation, consistent with a difference of 90° ± 10°.

4.2. Fiducial test cases

The three stars HD 027778, HD 108927, and HD 287150, selected in Sect. 4.1, have optical polarisation spectra and *Planck*-detected polarised emission measurements of grains from the same environment. They therefore serve as fiducial test cases to investigate the grain structure and alignment. We varied the axial ratio of the prolates for $n_{\rm a/b} = 5$ cases of $a/b \in \{1.5, 2.0, 2.5, 3.0, 4.0\}$ and adjusted the porosity, defined as the vacuum volume fraction, of the amorphous carbon and silicate grains for $n_{\rm Va} = 7$ cases of $V_{\rm a} \in \{0, 5, 10, 20, 30, 40, 50\}$ (%), as well as that of the micrometre-sized dust agglomerates for $n_{\rm V_{\mu A}} = 3$ cases of $V_{\mu\rm A} \in \{5, 10, 20\}$ (%). We computed the volume ratios of silicate ($V_{\rm Si}$), carbon ($V_{\rm C}$), and vacuum ($V_{\mu\rm A}$; i.e. porosity) in the fluffy micrometre-sized composites to match an abundance ratio of [Si]/[C] ∼ 3.6 (Hensley & Draine 2021). For the three porosity levels considered for the micrometre-sized dust, their cross-sections were computed using volume ratios $V_{\rm Si}$:$V_{\rm C}$:$V_{\mu\rm A}$ of 57:38:5, 53:37:10, and 48:32:20 (%).

We applied the simplified RAT alignment (Eq. (2)) unless stated otherwise. The silicate and dark-dust materials include Fe such that sufficiently large particles are perfectly aligned, $f_{\rm align} = 100\%$. For carbon, the situation is less clear: carbon grains are often assumed to be unaligned, $f_{\rm align} = 0$, while Herranen et al. (2021) and Andersson et al. (2024) find that grains without magnetic inclusions can reach $f_{\rm align} = 50\%$ through RAT alignment. We also experimented with perfect alignment of carbon grains but found that such models fail to reproduce most of the observations. In addition, we examined IDG alignment, noting that this theory neglects internal alignment. The aim is to assess whether IDG can be ruled out when fitting the data. The IDG efficiency parameter δ_0 typically varies from one sightline to another between $\delta_0 = 0.2$ and 1 µm (Das et al. 2010). The maximum alignment efficiency in IDG is approached asymptotically at $\delta_0 \gtrsim 10$ µm. This corresponds to alignment efficiencies of $f_{\rm align} = 18\%$ for $\delta_0 = 0.2$ µm, $f_{\rm align} = 32\%$ for $\delta_0 = 1$ µm, and 46% for $\delta_0 = 10$ µm. In total, we inspected $n_{f_{\rm align}} = 5$ levels of alignment efficiency. Within this sparsely sampled parameter space of $n_{\rm a/b} \times n_{\rm Va} \times n_{\rm V_{\mu A}} \times n_{f_{\rm align}} = 525$ models, we computed the dust cross-sections (Eqs. (7)–(5)) of prolate particles over 300 frequencies, 30 bins of $0° \lesssim \Omega < 90°$, and 130 radii ranging from 6 nm to 3 µm. In these models, a specific set of particle-structure parameters (a/b, $V_{\rm a}$, $V_{\mu\rm A}$) and alignment efficiency ($f_{\rm align}$) is applied uniformly across all grain types, and the fitting procedure described in Sect. 3.8 is used.

For each star, fits to the reddening curve that respect the elemental depletion constraints (Eq. (10)) and incorporate the *Gaia* distance estimates (Eq. (21)), together with the FORS starlight polarisation spectrum and the colour-corrected *Planck* total and polarised dust-emission spectrum, are presented in Fig. 2. The parameter set of the cross-sections with $a/b = 2$ and $V_{\rm a} = V_{\mu\rm A} = 10\%$ was adopted as the nominal model of the grain structure. In addition, for each star, two alternative models are shown that achieve a fit of comparable quality to the nominal model.

For HD 027778 and HD 108927, the best fits are obtained when neglecting the alignment of carbon grains, although for HD 027778 a comparably good fit is also achieved when assuming $f_{\rm align}$(aC) = 50%. In contrast, for HD 287150, aligned carbon grains make an important contribution to the optical polarisation and dominate the polarised emission. Models that ignore the alignment of aC grains for HD 287150 show a too-steep decline in the polarisation at $\lambda > 0.7$ µm to reproduce the optical polarisation spectrum, and they underpredict P_{850} by a factor of two. This underprediction of the polarisation in the optical and submillimetre can be compensated by a substantial increase in the mass of the micrometre-sized grains, which, however, leads to an overprediction of the near-IR reddening towards HD 287150.

In the optical, the polarisation cross-section $K_{\rm pol}$ can be dominated by aC grains if aligned, and otherwise by aSi grains. In this wavelength range, µA grains, if present, contribute only weakly, whereas they dominate $K_{\rm pol}$ at $\lambda > 1$ µm. Because aSi and µA grains attain similar temperatures, the polarised

Table 2. Dust parameters of the 27 sightlines that have been modelled.

1	2	3	4	5	6	7	8	9	10	11	12	13	14	15	16
Star	a/b	$V_{\rm vac}$	$m_{\mu A}$	$m_{\rm Si}$	$m_{\rm vSi}$ (%)	$m_{\rm aC}$	$m_{\rm vgr}$	$m_{\rm PAH}$	q	$r^-_{\rm pol,\,Si}$ (nm)	$r^-_{{\rm pol},aC}$	Ω (°)	$\frac{[Si]}{[H]}$ (ppm)	$\frac{[C]}{[H]}$ (ppm)	$\left(\frac{\tau_{s\mu}}{\tau_t}\right)_V$ (%)
HD 027778	2.0	10	25	37	28	5	3	1	2.3	112	–	38	42	78	20
HD 037903	2.0	10	33	31	18	13	4	1	2.1	143	69	50	32	108	37
HD 038023	1.5	5	32	37	19	8	2	2	2.6	25	–	53	38	88	34
HD 046223	1.5	5	30	33	24	8	4	1	2.6	136	–	63	37	91	29
HD 054439	1.5	5	–	58	21	13	5	3	2.8	112	69	27	38	93	0
HD 062542	1.5	5	25	28	35	8	3	1	2.8	143	–	76	49	110	22
HD 070614	2.0	10	–	52	22	18	6	2	2.5	143	42	47	34	109	0
HD 091824	2.0	10	41	33	14	9	2	1	2.3	102	–	51	36	96	52
HD 092044	2.0	10	34	36	19	8	2	1	2.6	112	88	39	38	89	48
HD 093222	1.5	5	35	34	13	15	2	1	2.5	30	–	41	32	110	38
HD 108927	2.0	10	30	32	20	13	4	1	2.0	97	–	46	33	106	23
HD 110946	2.0	10	19	39	27	10	4	1	2.8	143	54	49	37	92	9
HD 112607	1.5	5	–	39	39	13	6	3	2.7	143	–	37	35	96	0
HD 112954	2.0	10	8	32	44	10	5	1	2.5	183	54	60	43	94	1
HD 129557	1.5	5	35	44	12	3	4	2	2.0	102	–	47	41	81	42
HD 146285	1.5	5	39	31	10	15	4	1	2.0	143	69	61	28	114	33
HD 152245	1.5	5	35	38	14	8	3	2	2.6	112	88	40	37	91	44
HD 152249	1.5	5	63	21	9	5	1	1	2.3	201	92	40	38	94	44
HD 170740	1.5	5	–	46	29	16	6	3	2.8	183	26	72	35	103	0
HD 185418	1.5	5	27	43	13	10	5	2	2.5	112	88	32	35	98	19
HD 287150	2.0	10	17	32	34	13	3	1	2.8	143	8	36	36	97	6
HD 294304	1.5	5	27	36	23	10	3	1	2.7	102	–	34	37	95	23
HD 303308	2.0	10	26	38	23	9	3	1	2.4	112	88	52	39	88	20
HD 315021	1.5	5	33	40	10	13	3	1	2.4	118	–	30	35	103	35
HD 315023	1.5	5	32	38	11	15	2	2	2.5	143	88	53	33	108	32
HD 315024	1.5	5	67	15	7	8	2	1	2.3	47	–	53	45	170	46
HD 315032	2.0	5	34	33	17	11	4	1	2.3	112	–	16	34	104	43
median			31	37	19	10	3	1	2.5	118	69		37	96	32
sigma			16	8	9	4	1	1	0.3	23	25		4	17	17

Notes. For HD 091824 and HD 146285, the maximum grain size is $r_+ = 3\,\mu$m; otherwise, $r_+ = 1\,\mu$m. The derived C and Si abundances in the grains and the contribution of micrometre-sized dust agglomerates to the total optical depth are specified in Cols. 14–16. The median values and 1σ variations of the parameters are provided, excluding $r^-_{\rm pol,Si}$ for the two stars HD 038023 and HD 093222, as they exhibit peculiar polarisation spectra peaking in the B band.

emission in Fig. 2 is dominated by the micrometre-sized agglomerates when aC grains are not aligned. Notably, the optical and sub-millimetre polarisation arise from distinct grain populations. Following Fanciullo et al. (2015), we estimated the intensity scaling parameter (G_0) of the ISRF from *Planck* (Planck Collaboration XI 2014a) and IRAS observations, and the visual extinction A_V (Table A.1) to the stars. We find $G_0 = 0.56$, 0.37, and 0.43 for HD 027778, HD 108927, and HD 287150. No trend is found between aC alignment and G_0.

There are degeneracies in the model grid of particle structures, where multiple models match all datasets with similarly good quality. In Fig. 3, the total goodness of fit, $\chi^2_{\rm tot}$, normalised to the nominal model, is shown as a function of axial ratio and porosity. The contour levels at $\chi^2_{\rm tot} \lesssim 1$ highlight regions of comparable fit quality; these are marked in blue and correspond to models performing similarly to the nominal model (Fig. 3). Such models typically exhibit grain porosities $V_a \lesssim 20\,\%$ and axial ratios $a/b \lesssim 2.5$. The nominal model yields the lowest $\chi^2_{\rm tot}$ across the three stars for which both FORS spectra of the dichroic polarisation and *Planck* polarised-emission data are available. For these models, the upper radius of the grains, as derived from the *Planck* polarisation (Eqs. (19) and (20)), is $r^+_{\mu A} = 1\,\mu$m; the other model parameters are listed in Table 2.

4.3. Dust modelling of individual sightlines

The dust model is applied to the remaining 24 sightlines selected in Sect. 4.1, for which polarised emission data from the same grains responsible for the optical polarisation are not available. These stars are located at $|b| < 15°$, where the *Planck* observations suffer from low (40′) spatial resolution. The expected 90° flip in the polarisation angle between dichroic polarisation and polarised emission is also not observed (Table A.1).

The reddening curves and starlight polarisation spectra are fitted using Steps 1 and 2 of the fitting procedure (Sect. 3.8). The grain structures of the nominal model ($a/b = 2$, $V = 10\%$), together with the three other combinations of $a/b \in \{1.5, 2\}$ and $V \in \{5, 10\}(\%)$, are used. We adopted as default RAT alignment with perfectly aligned silicates, $f_{\rm align} = 100\%$, and include or exclude alignment of carbon grains with $f_{\rm align}({\rm aC}) \in \{0, 50\}\%$, as well as alignment of micrometre-sized dust with $f_{\rm align} = 100\%$. For comparison, IDG alignment is also applied using a size

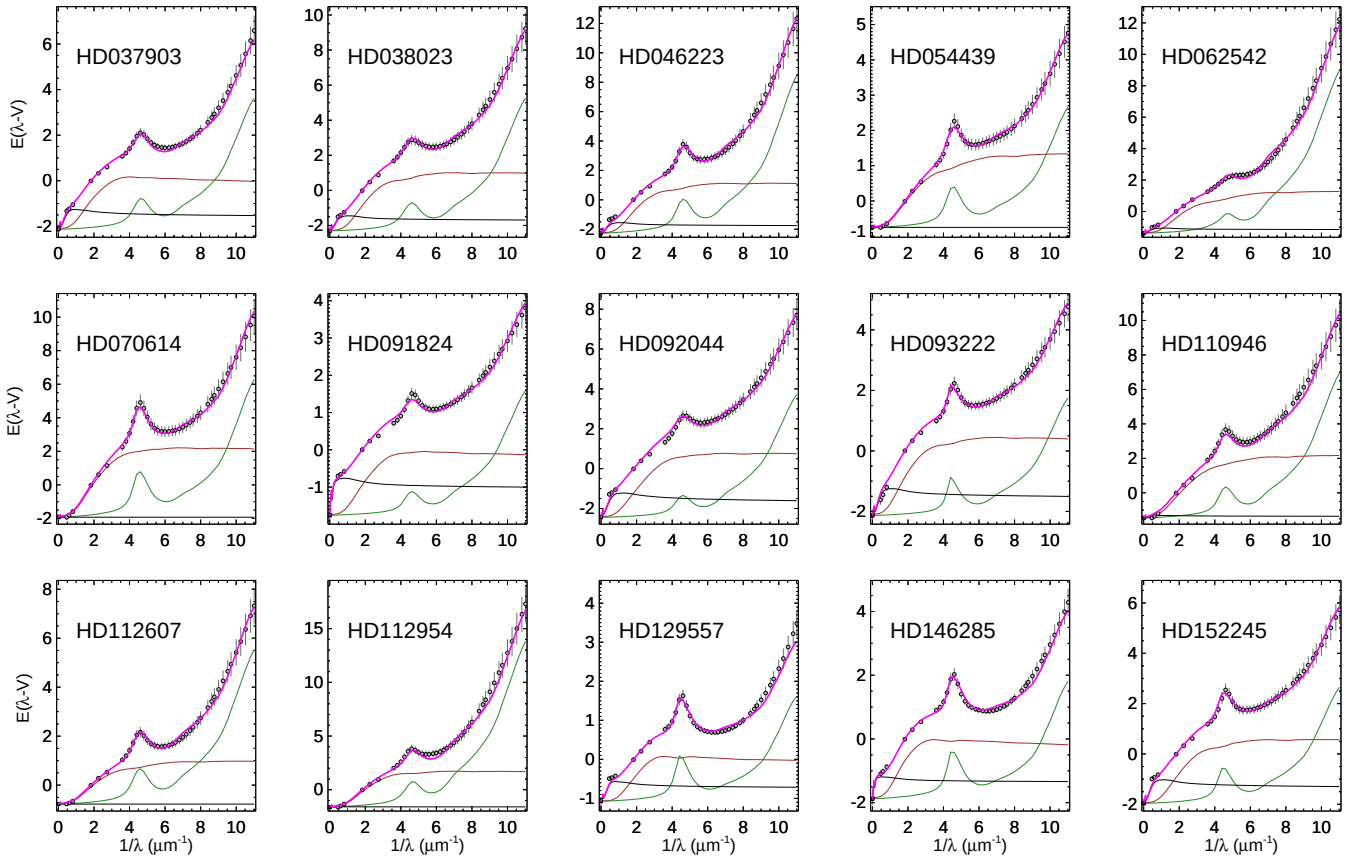

Fig. 4. Dust model fits to the absolute reddening curves, $E(\lambda - V)$, of 24 sightlines. Data (circles) cover 0.09–2.2 μm and are complemented at infinite wavelengths by $-A_V$ (Table A.1). The best fit, with contributions from nanoparticles (green), amorphous silicates and carbon grains (brown), and micrometre-sized dust agglomerates (dark), is shown, with the model parameters listed in Table 2. Notably, the micrometre-sized grains dominate in the IR and provide a wavelength-independent contribution in the optical and far-UV.

dependence similar to Eq. (2) (Siebenmorgen et al. 2014). The model fits and the contributions of the different grain components to the absolute reddening and the optical polarisation spectra are shown in Figs. 4 and 5, respectively.

The dust parameters and three derived quantities are listed for all 27 sightlines in Table 2. The axial ratios and porosities are given in Cols. 2 and 3. The model with $a/b = 2$ and a porosity of 10% is preferred for 11 sightlines (63%), while the model with $a/b = 1.5$ and a porosity of 5% provides a slightly lower $\chi^2_{\rm tot}$ for 16 sightlines. Except for two cases, the maximum grain radius is $r^+_{\mu A} = 1$ μm.

The relative masses $m_{\rm vgr}$, $m_{\rm vSi}$, $m_{\rm PAH}$, $m_{\rm aC}$, $m_{\rm aSi}$, and $m_{\mu A}$ in 1 g of dust (%) for the individual dust components are listed in Table 2, Cols. 4–9. The percentage contribution of the micrometre-sized grains to the total extinction in the optical is given in Col. 16. Typically, about one-third of the dust mass resides in micrometre-sized dust agglomerates, which also contribute about one-third of the total extinction $A_{\rm V}$ (Table 2).

The exponent of the dust size distribution q, the minimum alignment radii of amorphous silicate and carbon grains, $r^-_{\rm pol,Si}$ and $r^-_{\rm pol,aC}$, and the derived magnetic field orientation Ω are given in Table 2, Cols. 10–13. Additional derived quantities include the total Si and C abundances in dust relative to H (in ppm; Cols. 14–15). The typical abundances, [Si]/[H] ∼ 37 ppm and [C]/[H] ∼ 96 ppm, agree with estimates for the diffuse ISM by Hensley & Draine (2021). The median values and the 1σ scatter of the parameters are provided at the bottom of the table. The large scatter indicates substantial variation across individual sightlines.

As shown in Fig. 4, sightlines containing a significant amount of dark dust are dominated in the near-IR reddening by these micrometre-sized grains, which produce grey (constant) extinction in the optical. The amorphous grains produce a linear rise in extinction in the optical and add grey extinction in the far-UV. Nanoparticles are responsible for the 2175 Å extinction bump and the steep far-UV rise.

The polarisation spectra (Fig. 5) generally follow the Serkowski law with $\lambda_{\rm max}$ in the visible. Seven stars peak in the B band, and twelve stars peak at $\lambda_{\rm max} \gtrsim 0.65$ μm (Table A.1). The Serkowski fit is usually interpreted as tracing the characteristic size of aligned grains in a single absorbing cloud, although this is a simplification (Andersson et al. 2011). The polarisation results from the sum of contributions from silicate grains, dark dust, and (when aligned) amorphous carbon particles. These components peak at different wavelengths, and this could be caused by different clouds being located along the sightline (Mandarakas et al. 2025).

A noticeable deviation from the Serkowski curve is seen towards HD 093222, where the polarisation peaks at $\lambda_{\rm max} = 0.43$ μm and, after an initial decline, rises again at 0.7 μm towards the IR (Fig. 5). A strong wavelength gradient in the polarisation angle, $\mathrm{d}\theta/\mathrm{d}\lambda = 97°/\mu$m, is also observed (Table A.1).

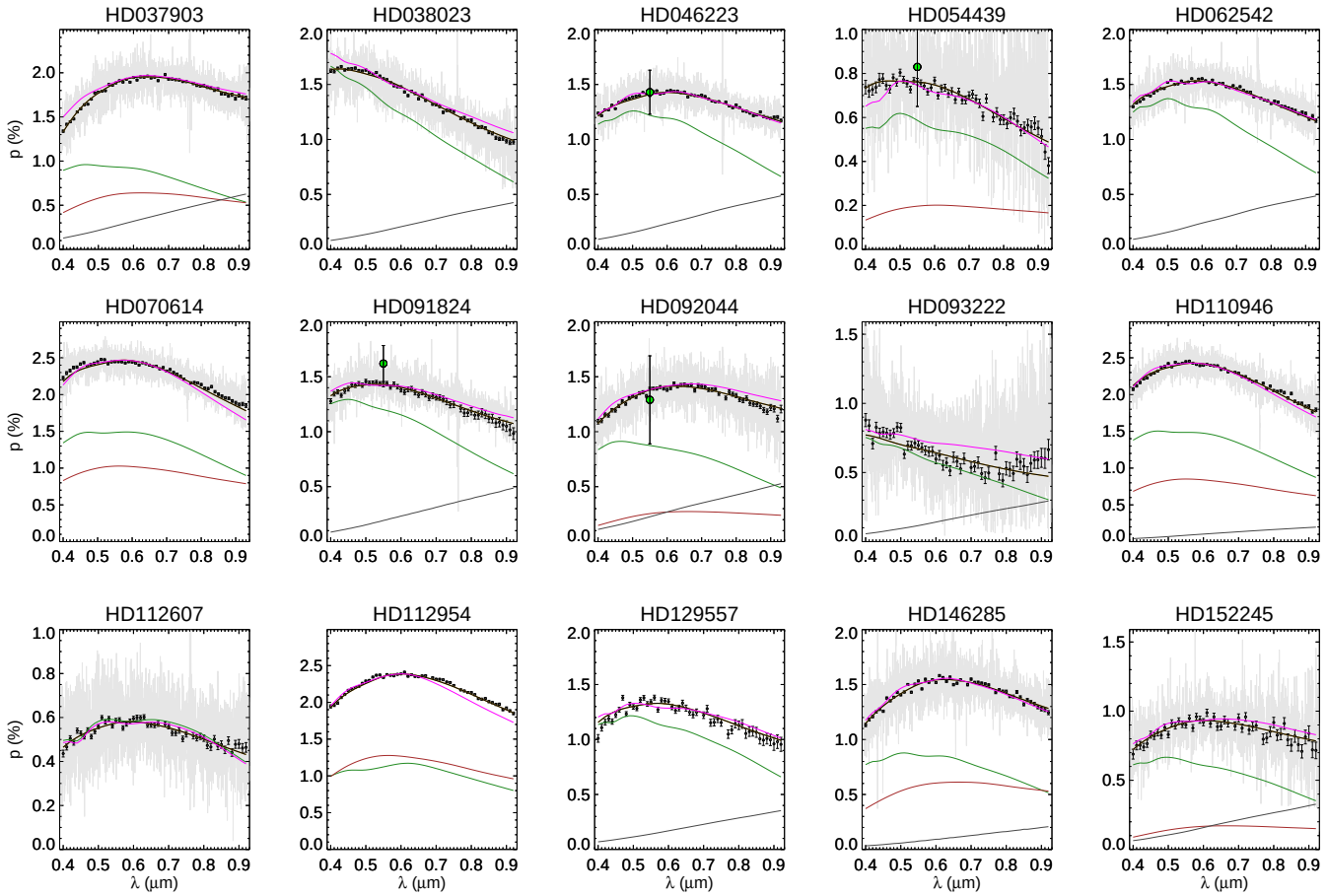

Fig. 5. Dust model fits to optical polarisation spectra obtained with FORS for 24 sightlines. Observations are shown as the original unbinned spectrum (grey lines) and re-binned to a spectral resolution of $\lambda/\Delta\lambda \sim 50$ (black open circles). The error bars associated with the re-binned spectra correspond to $1\,\sigma$. In each panel, best-fit dust models that adopt maximum IDG alignment efficiency are shown in ochre, while models based on RAT alignment are shown by the magenta line, with individual contributions from amorphous silicates (green line), carbon grains (brown line), and micrometre-sized dust agglomerates (black line) also indicated. Data available in the stellar polarisation catalogue by Heiles (2000) are shown with a green circle.

In a single-cloud scenario with a common magnetic field, the polarisation angle should remain constant and the polarisation should peak for typical ISM grain sizes at $\lambda_{\max} = 0.55\,\mu$m. Indeed, Mandarakas et al. (2025) reproduce the observed wavelength dependence of the polarisation angle towards HD 093222 using a two-cloud model. Two additional multiple-cloud sightlines in our sample, HD 037903 and HD 152245, show variations in polarisation angle, with $\mathrm{d}\theta/\mathrm{d}\lambda = 5.3$ and $6.8^\circ/\mu$m and maxima at $\lambda_{\max} = 0.66$ and $0.62\,\mu$m, respectively. Five single-cloud sightlines[2] show variations of $6.6 \lesssim \mathrm{d}\theta/\mathrm{d}\lambda \lesssim 18.5\ (^\circ/\mu\mathrm{m})$, while the remaining sightlines exhibit a weak wavelength dependence with $\mathrm{d}\theta/\mathrm{d}\lambda < 5^\circ/\mu$m (Table A.1, Fig. A.2).

The model fits the optical polarisation spectra typically within 1σ of the FORS data rebinned to $\lambda/\Delta\lambda \sim 50$ (Fig. 5). The contributions of the individual grain components to the optical polarisation spectra are shown in Fig. 5. Most of the polarisation, especially in the V band and at shorter wavelengths, is produced by silicate grains with a minimum alignment radius of $r^-_{\mathrm{pol,Si}} = 118 \pm 23$ nm. For half of the sightlines, the polarisation spectra are better reproduced when aligned carbon particles are included, with $r^-_{\mathrm{pol,aC}} = 69 \pm 25$ nm. The contribution from micrometre-sized grains rises steadily from $p \sim 0.1\%$ in the UV to $p \lesssim 0.5\%$ at $0.9\,\mu$m. These grains dominate the polarised emission in the (sub-)millimetre regime (Fig. 2).

The IDG model predicts lower alignment efficiency than RAT. Fits to the optical polarisation spectra using IDG systematically require the maximal alignment efficiency allowed by this model, with both silicate and carbon grains being aligned. Note that the lower alignment efficiencies in IDG are compensated in the fits (orange lines in Fig. 5) by increasing the axial ratio to typically $a/b = 2.5$, the porosity to 10%, and by overestimating the magnetic-field orientation Ω, typically by a factor of two.

5. Conclusion

We have completed the LIPS, which obtained FORS spectropolarimetry in the 0.38–0.92 μm wavelength range for 161 sightlines through the diffuse ISM. Sixty polarisation spectra are presented in this work. The LIPS sample was selected based on the availability of reddening curves: in the far-UV from the IUE and FUSE satellite missions, in the optical from ground-based photometry, and in the near-IR from 2MASS. High-resolution spectra were obtained with UVES/VLT to verify the spectral types and luminosity classes of the stars used for deriving the reddening curves and to probe the number of clouds along individual sightlines. *Gaia* parallaxes were used

[2] HD 054439, HD 046223, HD 092044, HD 038023, and HD 294304.

to estimate the visual extinction (A_V) necessary for reconciling the derived luminosity distances with the trigonometric distance estimates for the same stars. The starlight polarisation spectra were complemented by *Planck* 850 µm polarimetry.

This dataset was used to constrain the properties of grains in the diffuse ISM using a three-component model from Siebenmorgen (2023) that includes nanoparticles, amorphous grains, and micrometre-sized grains. The nanoparticles are responsible for the far-UV rise in the reddening curve, the 2175 Å bump, and the mid-IR emission bands. The amorphous grains produce grey (constant) extinction in the far-UV, an almost linear decline towards longer wavelengths, and the far-IR emission. The micrometre-sized particles contribute grey extinction in the optical, a linear decline in the near-IR, and the sub-millimetre emission. The optical polarisation is dominated by amorphous grains, while the 850 µm polarisation is dominated by the micrometre-sized dust agglomerates unless amorphous carbon particles are also aligned.

Within the sample, three sightlines exhibit both significant starlight and *Planck* polarisation, with comparable extinction values, $A_V^{850} \sim A_V$, and the expected 90° reversal in the polarisation angle between polarised emission and starlight polarisation. The polarisation data for these sightlines provide an almost orthogonal perspective on the aligned grains, enabling constraints to be placed on their particle shape, porosity, and alignment efficiency. Although degeneracies exist among the dust model parameters, a good fit to all data for these three sightlines is obtained using an axial ratio $a/b = 2$ and porosities of 10% for both the amorphous and micrometre-sized grains.

We applied RAT (Hoang & Lazarian 2016) in the simplified formulation from Reissl et al. (2020), assuming perfect alignment for silicate and micrometre-sized dust. For carbon grains, we considered two cases, either including alignment with $f_{\rm align}$(aC) = 50% or assuming no alignment. This nominal model was applied to 24 additional sightlines for which high-quality reddening curves and optical polarisation spectra were available but for which the *Planck* polarisation data were ambiguous. For half of these sightlines, the best fits include aligned carbon grains. A single-cloud model generally provides fits consistent within the 1σ uncertainties. The IDG models, which ignore internal alignment, reproduce the optical polarisation only when forced to their asymptotic maximum alignment for both silicate and carbon grains, at the cost of overestimating parameters such as the magnetic field orientation (Ω).

The contribution of micrometre-sized dust is most evident in the near-IR extinction and, with few exceptions, is marginal in the optical spectropolarimetry. Overall, we find that micrometre-sized dust is responsible for approximately one-third of the total extinction and comprises one-third of the total dust mass. Significant variations in dust abundances persist from cloud to cloud.

The present analysis is limited by the low spatial resolution of the *Planck* maps, which leads to source confusion. A follow-up sub-millimetre survey with a high-spatial-resolution polarimeter is required, once it becomes available, to combine polarised emission and starlight polarisation measurements through the diffuse ISM.

Data availability

The Fortran code of the dust model described in Siebenmorgen & Heymann (2026a) and the corresponding library of dust cross-sections for spheroidal grains (Siebenmorgen & Heymann 2026b) are publicly available. The processed FORS polarisation spectra presented in this work are available at the CDS via https://cdsarc.cds.unistra.fr/viz-bin/cat/J/A+A/709/A277

Acknowledgements. We thank the referee for the valuable and constructive comments, in particular regarding the consideration of radiative torque alignment (RAT) theory. This research has made use of the services of the ESO Science Archive Facility and of the SIMBAD database, operated at the CDS, Strasbourg, France. This work is partially based on observations collected at the European Southern Observatory under ESO programme 102.C-0040.

References

Allamandola, L. J., Tielens, A. G. G. M., & Barker, J. R. 1989, ApJS, 71, 733
Andersson, B.-G., Pintado, O., Potter, S. B., Straižys, V., & Charcos-Llorens, M. 2011, A&A, 534, A19
Andersson, B.-G., Lazarian, A., & Vaillancourt, J. E. 2015, ARA&A, 53, 501
Andersson, B.-G., Karoly, J., Bastien, P., et al. 2024, ApJ, 963, 76
Appenzeller, I., Fricke, K., Fürtig, W., et al. 1998, The Messenger, 94, 1
Bagnulo, S., Cox, N. L. J., Cikota, A., et al. 2017, A&A, 608, A146
Bailer-Jones, C. A. L., Rybizki, J., Fouesneau, M., Demleitner, M., & Andrae, R. 2021, AJ, 161, 147
Bianchi, S. 2024, A&A, 691, A330
Blasberger, A., Behar, E., Perets, H. B., Brosch, N., & Tielens, A. G. G. M. 2017, ApJ, 836, 173
Bohlin, R. C., Savage, B. D., & Drake, J. F. 1978, ApJ, 224, 132
Bohren, C. F., & Huffman, D. R. 1983, Absorption and Scattering of Light by Small Particles, Research supported by the University of Arizona and Institute of Occupational and Environmental Health (New York, Wiley-Interscience), 1983, 541
Bowen, D. V., Jenkins, E. B., Tripp, T. M., et al. 2008, ApJS, 176, 59
Chini, R., Krügel, E., Haslam, C. G. T., et al. 1993, A&A, 272, L5
Chini, R., Krügel, E., Lemke, R., & Ward-Thompson, D. 1995, A&A, 295, 317
Cutri, R. M., Skrutskie, M. F., van Dyk, S., et al. 2003, 2MASS All Sky Catalog of point sources. (ADS)
Das, H. K., Voshchinnikov, N. V., & Il'in, V. B. 2010, MNRAS, 404, 265
Davis, Jr., L., & Greenstein, J. L. 1951, ApJ, 114, 206
Dekker, H., D'Odorico, S., Kaufer, A., Delabre, B., & Kotzlowski, H. 2000, SPIE Conf. Ser., 4008, 534
Demyk, K., Gromov, V., Meny, C., et al. 2022, A&A, 666, A192
Diplas, A., & Savage, B. D. 1994, ApJ, 427, 274
Dolginov, A. Z., & Mitrofanov, I. G. 1976, Ap&SS, 43, 291
Dorschner, J., Begemann, B., Henning, T., Jaeger, C., & Mutschke, H. 1995, A&A, 300, 503
Draine, B. T. 2003, ApJ, 598, 1017
Draine, B. T., & Fraisse, A. A. 2009, ApJ, 696, 1
Draine, B. T., & Hensley, B. S. 2021, ApJ, 909, 94
Draine, B. T., & Weingartner, J. C. 1996, ApJ, 470, 551
Ensor, T., Cami, J., Bhatt, N. H., & Soddu, A. 2017, ApJ, 836, 162
Fanciullo, L., Guillet, V., Aniano, G., et al. 2015, A&A, 580, A136
Fitzpatrick, E. L., & Massa, D. 2007, ApJ, 663, 320
Gaia Collaboration (Vallenari, A., et al.) 2023, A&A, 674, A1
Galametz, M., Madden, S., Galliano, F., et al. 2009, A&A, 508, 645
Galliano, F., Madden, S. C., Jones, A. P., Wilson, C. D., & Bernard, J. P. 2005, A&A, 434, 867
Giang, N. C., Le Gouellec, V. J. M., Hoang, T., Maury, A. J., & Hennebelle, P. 2025, ApJ, 980, 105
Gordon, K. D., Cartledge, S., & Clayton, G. C. 2009, ApJ, 705, 1320
Guhathakurta, P., & Draine, B. T. 1989, ApJ, 345, 230
Guillet, V., Fanciullo, L., Verstraete, L., et al. 2018, A&A, 610, A16
Hall, J. S. 1949, Science, 109, 166
Heiles, C. 2000, AJ, 119, 923
Hensley, B. S., & Draine, B. T. 2021, ApJ, 906, 73
Herranen, J., Lazarian, A., & Hoang, T. 2021, ApJ, 913, 63
Hildebrand, R. H. 1988, QJRAS, 29, 327
Hiltner, W. A. 1949, Science, 109, 165
Hoang, T., & Lazarian, A. 2016, ApJ, 831, 159
Hoang, T., & Truong, B. 2024, ApJ, 965, 183
Hoang, T., Tram, L. N., Lee, H., Diep, P. N., & Ngoc, N. B. 2021, ApJ, 908, 218
Hong, S. S., & Greenberg, J. M. 1980, A&A, 88, 194
Jones, R. V., & Spitzer, Jr., L. 1967, ApJ, 147, 943
Kennicutt, R. C., Calzetti, D., Aniano, G., et al. 2011, PASP, 123, 1347
Kim, S.-H., & Martin, P. G. 1995, ApJ, 444, 293
Krügel, E. 2008, An Introduction to the Physics of Interstellar Dust (UK: IOP)
Krügel, E., & Siebenmorgen, R. 1994, A&A, 288, 929
Krügel, E., Siebenmorgen, R., Zota, V., & Chini, R. 1998, A&A, 331, L9
Krüger, H., Strub, P., Grün, E., & Sterken, V. J. 2015, ApJ, 812, 139

Landgraf, M., Baggaley, W. J., Grün, E., Krüger, H., & Linkert, G. 2000, J. Geophys. Res., 105, 10343
Lazarian, A. 1997, MNRAS, 288, 609
Lazarian, A., & Hoang, T. 2007, MNRAS, 378, 910
Lenz, D., Hensley, B. S., & Doré, O. 2017, ApJ, 846, 38
Liszt, H. 2014, ApJ, 780, 10
Luri, X., Brown, A. G. A., Sarro, L. M., et al. 2018, A&A, 616, A9
Madden, S. C., Rémy-Ruyer, A., Galametz, M., et al. 2013, PASP, 125, 600
Maíz Apellániz, J. 2022, A&A, 657, A130
Mandarakas, N., Tassis, K., & Skalidis, R. 2025, A&A, 698, A168
Mathis, J. S., Mezger, P. G., & Panagia, N. 1983, A&A, 128, 212
Mathis, J. S., Rumpl, W., & Nordsieck, K. H. 1977, ApJ, 217, 425
Nguyen, H., Dawson, J. R., Miville-Deschênes, M. A., et al. 2018, ApJ, 862, 49
Ormel, C. W., Min, M., Tielens, A. G. G. M., Dominik, C., & Paszun, D. 2011, A&A, 532, A43
Planck Collaboration XI. 2014a, A&A, 571, A11
Planck Collaboration XVII. 2014b, A&A, 566, A55
Planck Collaboration XIX. 2015a, A&A, 576, A104
Planck Collaboration XXI. 2015b, A&A, 576, A106
Planck Collaboration XII. 2020, A&A, 641, A12
Popovic, B., Wiseman, P., Sullivan, M., et al. 2024, MNRAS, 534, 2263
Puget, J. L., & Leger, A. 1989, ARA&A, 27, 161
Purcell, E. M. 1979, ApJ, 231, 404
Rachford, B. L., Snow, T. P., Destree, J. D., et al. 2009, ApJS, 180, 125
Reissl, S., Guillet, V., Brauer, R., et al. 2020, A&A, 640, A118
Rémy-Ruyer, A., Madden, S. C., Galliano, F., et al. 2013, A&A, 557, A95
Roberge, W. G., & Lazarian, A. 1999, MNRAS, 305, 615
Serkowski, K., Mathewson, D. S., & Ford, V. L. 1975, ApJ, 196, 261
Siebenmorgen, R. 2023, A&A, 670, A115
Siebenmorgen, R. 2025, https://doi.org/10.5281/zenodo.14624100
Siebenmorgen, R., & Heymann, F. 2026a, https://doi.org/10.5281/zenodo.19190239
Siebenmorgen, R., & Heymann, F. 2026b, https://doi.org/10.5281/zenodo.19236224
Siebenmorgen, R., Heymann, F., & Chini, R. 2025, ApJ, 979, L45
Siebenmorgen, R., Kruegel, E., & Mathis, J. S. 1992, A&A, 266, 501
Siebenmorgen, R., Krügel, E., & Chini, R. 1999, A&A, 351, 495
Siebenmorgen, R., Voshchinnikov, N. V., & Bagnulo, S. 2014, A&A, 561, A82
Siebenmorgen, R., Voshchinnikov, N. V., Bagnulo, S., et al. 2018, A&A, 611, A5
Siebenmorgen, R., Krełowski, J., Smoker, J., Galazutdinov, G., & Bagnulo, S. 2020, A&A, 641, A35
Siebenmorgen, R., Smoker, J., Krełowski, J., Gordon, K., & Chini, R. 2023, A&A, 676, A132
Smoker, J., Haddad, N., Iwert, O., et al. 2009, The Messenger, 138, 8
Stecher, T. P., & Donn, B. 1965, ApJ, 142, 1681
Vaillancourt, J. E., Andersson, B. G., Clemens, D. P., et al. 2020, ApJ, 905, 157
Valencic, L. A., Clayton, G. C., & Gordon, K. D. 2004, ApJ, 616, 912
Voshchinnikov, N. V. 2004, Astrophys. Space Phys. Res., 12, 1
Voshchinnikov, N. V. 2012, J. Quant. Spec. Radiat. Transf., 113, 2334
Voshchinnikov, N. V., & Farafonov, V. G. 1993, Ap&SS, 204, 19
Wang, S., Li, A., & Jiang, B. W. 2015a, MNRAS, 454, 569
Wang, S., Li, A., & Jiang, B. W. 2015b, ApJ, 811, 38
Wegner, W. 2006, MNRAS, 371, 185
Westphal, A. J., Stroud, R. M., Bechtel, H. A., et al. 2014, Science, 345, 786
Ysard, N., Jones, A. P., Guillet, V., et al. 2024, A&A, 684, A34
Zubko, V. G., Mennella, V., Colangeli, L., & Bussoletti, E. 1996, MNRAS, 282, 1321

Appendix A: Tables and figures

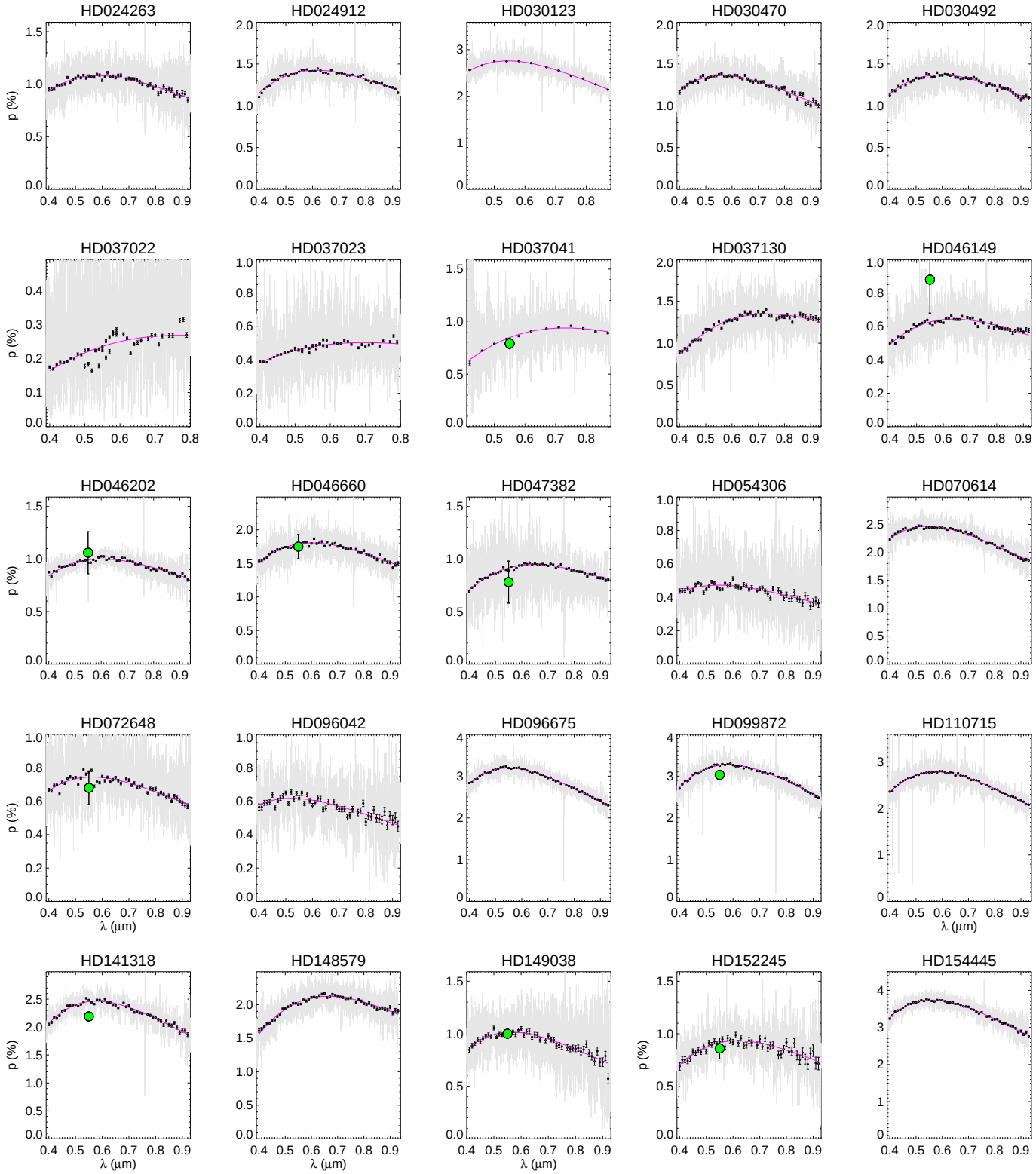

Fig. A.1. FORS polarisation spectra of 43 stars. The grey lines show the original data, and the black open circles (with 1 σ error bars) represent the data re-binned to a spectral resolution of $\lambda/\Delta\lambda \sim 50$. The green circles represent the measurements available in the catalogue by Heiles (2000). The magenta lines show the best fits obtained with the Serkowski formula.

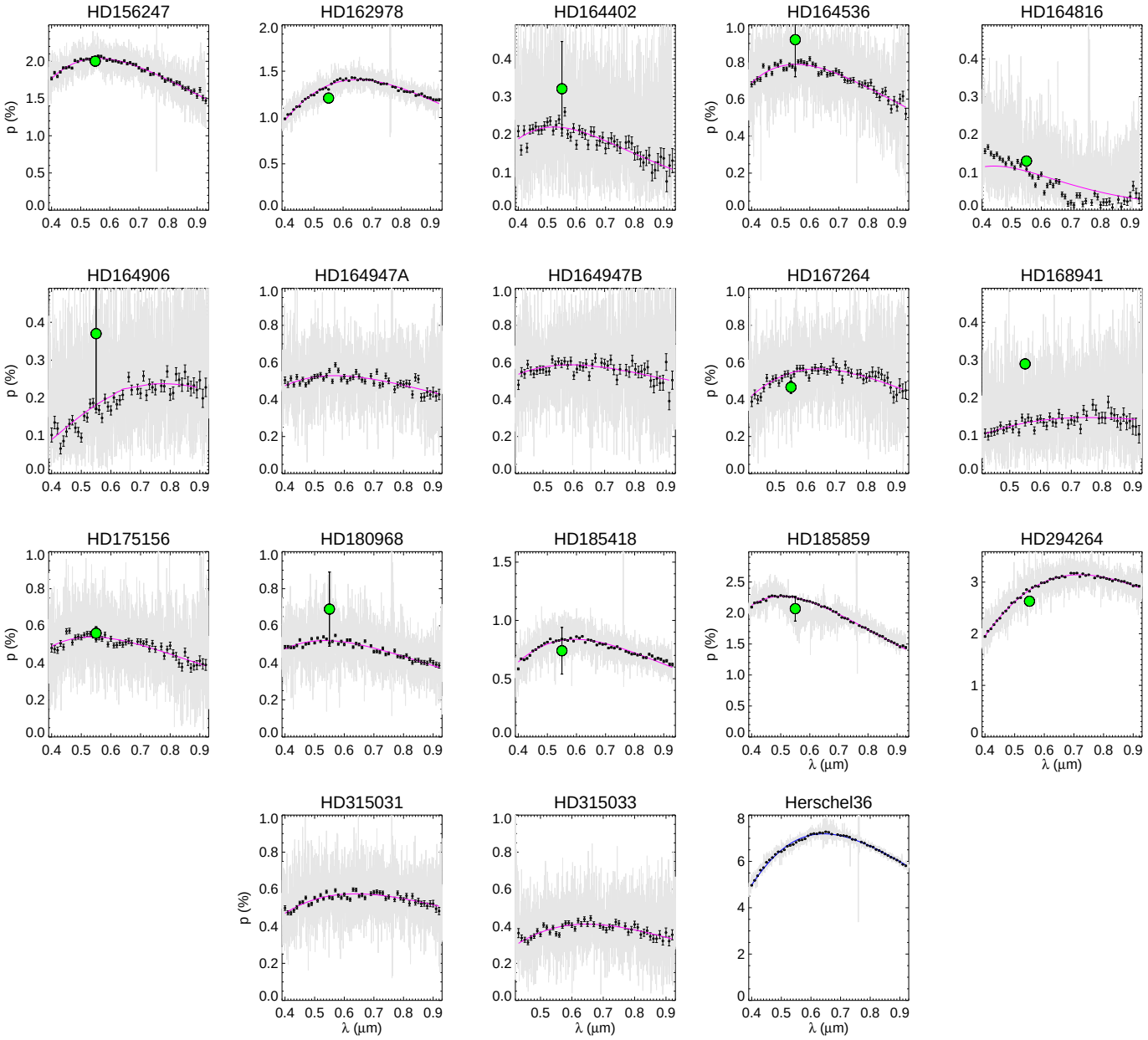

Fig. A.1. continued.

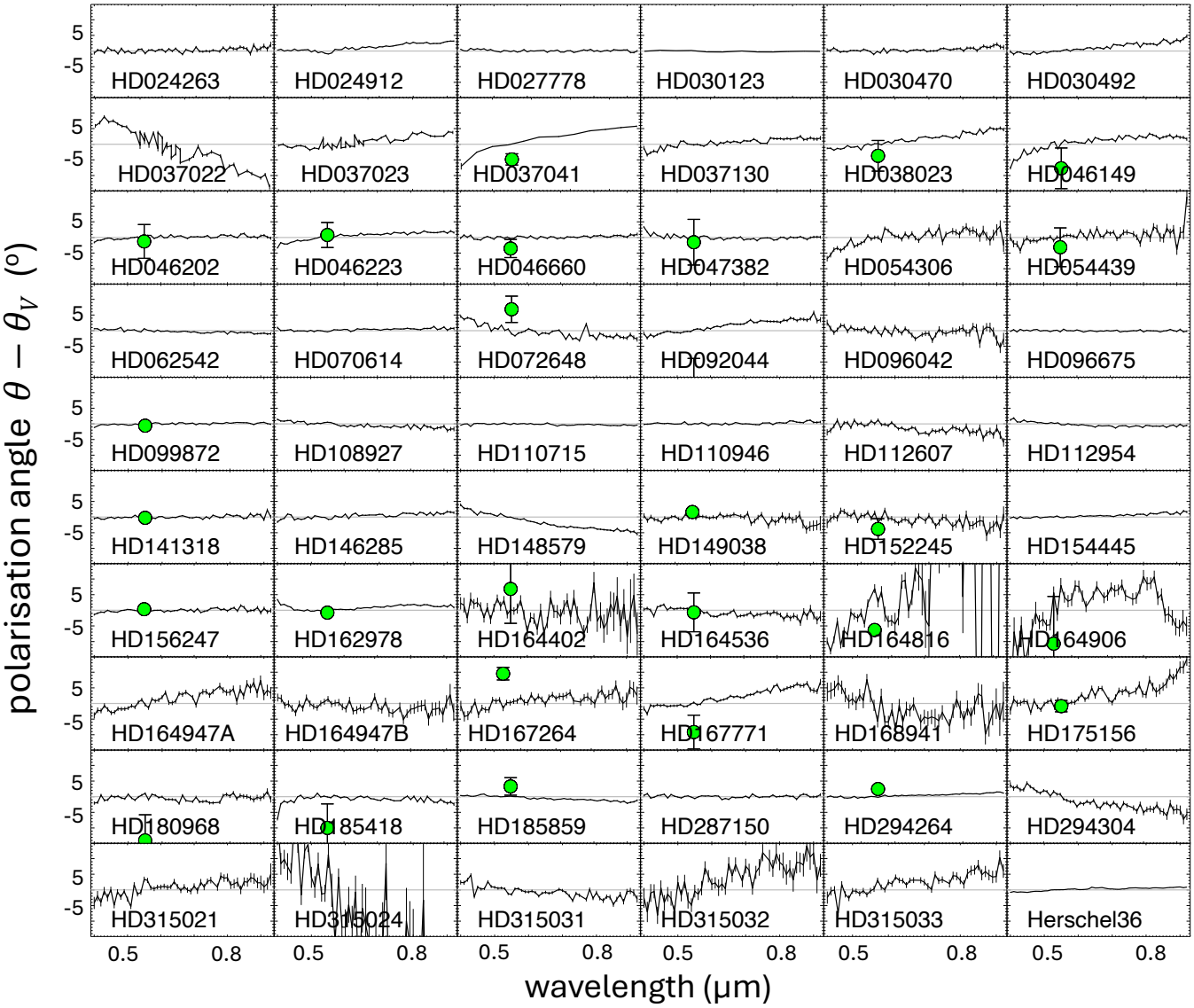

Fig. A.2. Position angle of the polarisation for the 60 stars in the LIPS sample analysed in this work, offset with respect to its value in the V optical filter, $\theta - \theta_V$ (see Table A.1). Data available in the catalogue by Heiles (2000) are shown with green circles.

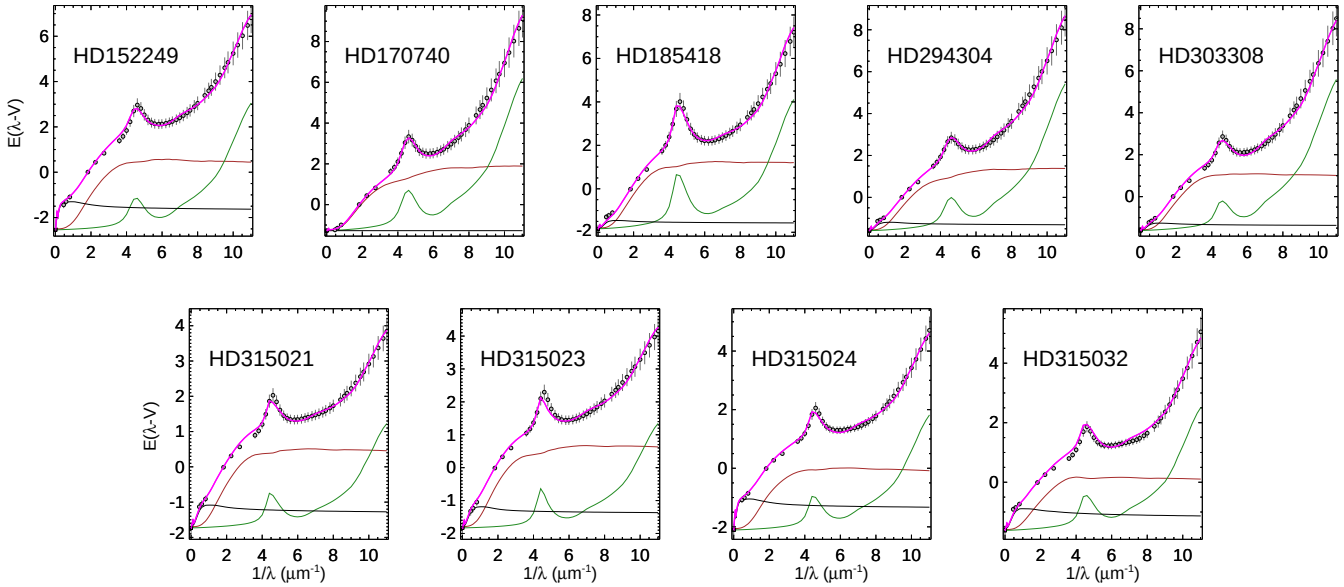

Fig. A.3. Dust model fits to the absolute reddening curves, continued from Fig. 4.

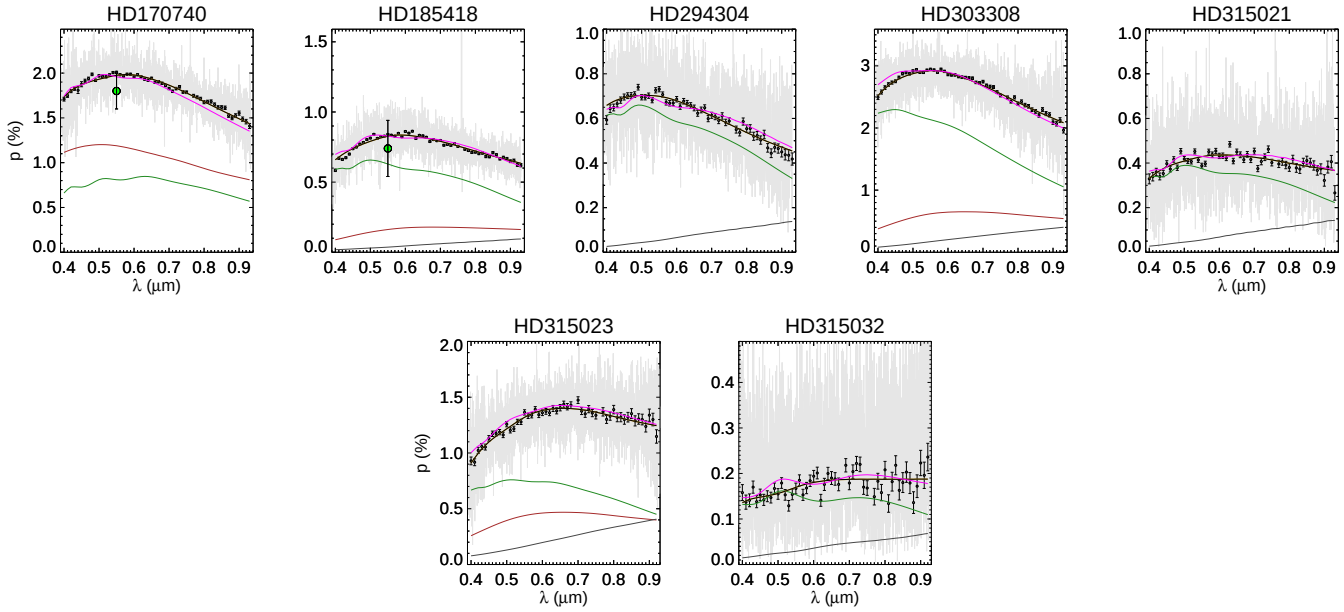

Fig. A.4. FORS polarisation spectra and models, continued from Fig. 5.

Table A.1. Stars with derived *Planck*, reddening, FORS, and Serkowski fit parameters.

1	2	3	4	5	6	7	8	9	10	11	12	13	14	15	16	17
Star		*Planck*				Reddening				FORS				Serkowski		
Name	$\|\|b\|\|$	I_{850} MJy/sr	p_{850} %	θ_{850} °	A_V^{850} mag	A_V mag	$A_V^{\rm ref}$ mag	Ref	SM	Date	p_V %	θ_V °	$\mathrm{d}\theta/\mathrm{d}\lambda$ °/µm	$p_{\max}$ %	$\lambda_{\max}$ µm	$k_{\rm pol}$
HD 024263	35	1.00	6.0± 2.4	77± 18	0.8	–	0.7	V	S	2019-02-24	1.1 ± 0.1	149 ± 0.5	2 ± 0.7	1.08	0.58	1.04
HD 024912	13	1.28	6.9± 2.4	27± 6	1.1	–	1.0	V	M	2015-12-25	1.4 ± 0.1	111 ± 0.6	7 ± 1.1	1.43	0.62	1.16
”										2018-11-17						
”										2018-11-17						
HD 027778	17	1.33	6.5± 2.4	152± 7	1.2	1.2	1.1	G	M	2015-12-23	1.6 ± 0.1	69 ± 0.3	-1 ± 0.3	1.65	0.52	1.08
”										2018-11-14						
HD 030123	17	1.96	6.8± 2.4	179± 4	1.6	–	1.6	F	M	2020-10-02	2.8 ± 0.1	85 ± 0.2	-1 ± 0.2	2.76	0.54	1.14
HD 030470	21	1.26	6.5± 2.7	178± 12	1.1	–	1.1	F	S	2019-03-17	1.4 ± 0.1	76 ± 0.5	2 ± 0.6	1.36	0.56	1.20
HD 030492	21	1.26	6.7± 2.8	171± 4	1.1	–	1.2	F	S	2019-03-18	1.4 ± 0.1	77 ± 0.4	9 ± 1.5	1.37	0.59	1.16
HD 037022	19	353	2.9± 2.7	40± 16	294	–	1.9	F	S	2015-12-23	0.2 ± 0.1	146 ± 2.9	-52 ± 5.7	0.27	0.77	1.25
”										2020-10-02						
HD 037023	19	353	2.9± 2.7	40± 68	294	–	1.7	V	S	2015-12-23	0.5 ± 0.1	61 ± 1.3	13 ± 1.7	0.51	0.71	0.82
”										2020-10-01						
HD 037041	19	255	2.7± 2.6	40± 29	212	–	1.1	V	S	2020-10-25	0.8 ± 0.1	101 ± 0.7	20 ± 3.6	0.94	0.72	1.45
HD 037130	19	5.34	7.4± 2.3	30± 17	4.5	–	1.3	F	S	2019-03-18	1.2 ± 0.1	138 ± 0.7	7 ± 1.4	1.35	0.74	1.17
HD 037367	1	4.46	4.7± 4.7	70± 35	3.7	–	1.5	V	M	B17	1.0 ± 0.1	15 ± 0.9	0 ± 1.2	1.02	0.63	1.13
HD 037903	17	35.4	2.2± 2.0	65± 34	30	–	1.5	G	M	2015-12-25	1.9 ± 0.1	121 ± 0.3	5 ± 0.9	1.96	0.66	1.42
”										2018-11-12						
HD 038023	19	11.7	3.8± 2.0	20± 23	9.7	2.3	1.6	F	S	2019-02-23	1.6 ± 0.1	87 ± 0.7	13 ± 2.1	1.64	0.43	0.93
”										2019-03-18						
HD 046149	2	4.89	4.6± 2.1	65± 30	4.1	–	1.3	F	M	2018-12-07	0.6 ± 0.1	5 ± 1.0	13 ± 2.4	0.64	0.64	1.17
HD 046202	2	4.85	4.2± 2.1	62± 26	4.0	–	1.5	G	M	2018-12-08	1.0 ± 0.1	178 ± 0.5	2 ± 0.5	1.00	0.60	1.05
HD 046223	2	6.26	4.2± 2.1	64± 14	5.2	2.3	1.5	V	S	2018-12-07	1.4 ± 0.1	168 ± 0.6	8 ± 1.2	1.43	0.59	1.05
HD 046660	1	3.75	5.6± 2.3	87± 19	3.1	–	1.7	F	M	2020-10-02	1.8 ± 0.1	17 ± 0.3	1 ± 0.4	1.81	0.60	1.09
HD 047382	1	3.76	5.8± 2.0	69± 5	3.1	–	1.4	F	M	2018-12-11	0.9 ± 0.1	155 ± 0.6	-2 ± 0.8	0.95	0.65	1.28
”										2018-12-14						
HD 054306	2	3.39	3.4± 1.9	56± 2	2.8	–	0.6	F	M	2019-02-23	0.5 ± 0.1	147 ± 1.5	12 ± 2.3	0.47	0.55	0.98
HD 054439	2	3.07	3.3± 1.9	56± 7	2.6	0.7	0.8	F	S	2015-12-23	0.8 ± 0.1	139 ± 0.6	7 ± 2.3	0.77	0.51	1.17
HD 062542	9	3.17	0.3± 1.4	147± 31	2.6	1.4	1.2	G	S	2018-12-07	1.5 ± 0.1	26 ± 0.3	-3 ± 0.5	1.53	0.58	1.21
HD 070614	3	5.87	2.2± 1.5	32± 65	4.9	–	2.1	F	M	2019-02-06	2.4 ± 0.1	58 ± 0.2	2 ± 0.4	2.47	0.54	1.01
HD 072648	2	7.38	0.1± 1.6	57± 36	6.1	–	1.2	F	M	2019-02-24	0.7 ± 0.1	3 ± 0.9	-11 ± 2.0	0.74	0.56	1.03
”										2019-03-17						
HD 073882	1	10.8	1.7± 0.2	72± 2	9.0	–	2.5	G	M	B17	1.9 ± 0.1	164 ± 0.5	-1 ± 0.8	2.08	0.69	1.30
HD 075309	2	5.05	2.3± 1.6	114± 31	4.2	–	0.9	F	M	B17	0.6 ± 0.1	54 ± 1.9	-7 ± 3.6	0.62	0.51	1.33
HD 079186	2	3.89	1.0± 1.6	102± 36	3.2	–	1.3	V	S	B17	2.6 ± 0.1	47 ± 0.3	-2 ± 0.5	2.61	0.52	1.19
HD 089137	4	1.14	3.1± 1.7	101± 28	0.9	–	0.7	V	S	2019-02-06	0.4 ± 0.1	39 ± 1.3	-4 ± 1.6	0.41	0.64	1.09
HD 091824	0	16.0	2.3± 1.6	20± 13	13	–	0.8	F	M	2018-12-14	1.4 ± 0.1	97 ± 0.4	4 ± 0.8	1.43	0.53	1.08
HD 091983	0	17.6	1.0± 1.5	74± 33	15	–	0.9	F	S	B17	1.1 ± 0.1	131 ± 1.0	18 ± 3.2	1.11	0.56	0.95
HD 092044	0	18.8	2.0± 1.5	89± 19	16	2.4	1.4	F	S	2020-10-04	1.4 ± 0.1	160 ± 0.5	12 ± 1.9	1.42	0.63	1.33
HD 093205	1	33.5	0.3± 1.5	17± 8	28	–	1.2	V	M	B17	2.1 ± 0.1	100 ± 0.4	-5 ± 1.0	2.10	0.55	1.16
HD 093222	1	22.0	0.2± 1.4	55± 11	18	–	1.8	G	M	B17	0.7 ± 0.1	134 ± 3.9	97 ± 12.2	0.77	0.43	1.45
HD 093632	1	28.5	1.0± 1.4	151± 8	24	–	2.3	V	M	B17	1.1 ± 0.1	53 ± 1.1	-20 ± 4.9	1.47	0.84	1.29
HD 094493	1	11.6	0.3± 1.4	146± 51	9.7	–	0.8	V	M	B17	0.6 ± 0.1	107 ± 2.2	12 ± 4.5	0.67	0.43	1.04
HD 096042	1	7.68	1.8± 1.5	97± 73	6.4	–	0.9	V	M	2015-01-02	0.6 ± 0.1	115 ± 0.9	-4 ± 1.5	0.61	0.52	0.85
HD 096675	15	1.76	10.6± 1.4	19± 21	1.5	–	1.0	G	S	2019-03-14	3.2 ± 0.1	130 ± 0.2	0 ± 0.2	3.19	0.55	1.20
HD 097484	1	11.0	1.2± 1.4	44± 74	9.2	–	1.5	V	M	B17	0.9 ± 0.1	60 ± 1.4	10 ± 2.2	0.96	0.52	1.18
HD 099872	11	1.28	13.9± 1.5	31± 3	1.1	–	1.1	G	M	S14	3.2 ± 0.1	118 ± 0.3	1 ± 0.3	3.27	0.58	1.27
”										2019-03-09						
HD 103779	1	10.8	1.8± 1.6	170± 5	9.0	–	0.7	G	M	B17	0.6 ± 0.1	75 ± 1.7	-26 ± 5.2	0.62	0.52	1.76
HD 104705	0	17.0	1.2± 2.0	66± 70	14	–	1.2	F	S	B17	0.8 ± 0.2	86 ± 3.5	-7 ± 7.2	0.77	0.62	0.89
HD 108927	15	0.92	7.4± 1.8	29± 3	0.8	1.1	0.7	F	S	2019-03-09	1.5 ± 0.1	122 ± 0.4	-5 ± 0.8	1.53	0.52	1.15
HD 110715	2	5.12	5.9± 2.3	168± 3	4.3	–	1.3	F	S	2019-03-08	2.8 ± 0.1	75 ± 0.2	-1 ± 0.3	2.79	0.58	1.28
”										2019-03-14						
HD 110946	2	5.10	5.4± 2.1	166± 3	4.3	1.5	1.6	F	S	2019-02-11	2.4 ± 0.1	79 ± 0.3	1 ± 0.4	2.43	0.56	1.30
HD 112607	1	16.7	1.5± 2.5	146± 6	14	0.7	0.8	F	S	2019-03-04	0.6 ± 0.1	63 ± 0.6	-7 ± 1.5	0.58	0.59	1.47
HD 112954	0	29.2	0.4± 2.2	41± 87	24	1.5	1.7	F	S	2019-02-24	2.3 ± 0.1	45 ± 0.3	-4 ± 0.7	2.39	0.60	1.35
HD 122879	2	8.07	2.0± 1.9	173± 13	6.7	–	1.1	V	M	B17	1.8 ± 0.1	70 ± 0.5	-5 ± 0.9	1.81	0.55	1.52
HD 129557	4	2.32	6.2± 2.0	171± 0	1.9	1.1	0.5	V	S	B17	1.3 ± 0.1	80 ± 0.7	1 ± 1.0	1.33	0.57	1.54
HD 134591	20	0.76	4.2± 2.3	131± 73	0.6	–	0.6	V	M	B17	0.3 ± 0.1	114 ± 5.4	24 ± 11.6	0.31	0.43	0.54
HD 141318	1	33.8	2.5± 2.3	149± 8	28	–	0.8	V	M	2014-10-10	2.4 ± 0.1	51 ± 0.2	1 ± 0.5	2.46	0.58	1.27
HD 146285	18	2.12	4.9± 2.6	123± 15	1.8	1.9	1.2	F	S	2019-03-19	1.5 ± 0.1	18 ± 0.5	4 ± 0.8	1.55	0.63	1.47
HD 147888	18	4.59	7.2± 2.5	132± 12	3.8	–	2.0	G	S	B17	3.3 ± 0.1	54 ± 0.2	-3 ± 0.6	3.49	0.66	1.49
HD 147889	17	17.6	1.1± 2.6	123± 37	15	–	4.3	V	S	B17	3.4 ± 0.2	177 ± 0.4	-7 ± 1.4	4.20	0.81	1.30
HD 148379	2	8.01	1.8± 2.3	132± 12	6.7	–	2.4	V	M	B17	1.9 ± 0.1	30 ± 0.6	-1 ± 0.7	1.95	0.58	0.94
HD 148579	16	3.91	2.5± 2.5	139± 30	3.3	–	1.4	F	S	2021-01-23	2.0 ± 0.1	79 ± 0.7	-15 ± 2.4	2.12	0.66	1.16
HD 149038	3	5.42	1.4± 2.4	161± 43	4.5	–	1.1	V	M	2019-04-02	1.0 ± 0.1	29 ± 0.6	-1 ± 1.2	1.02	0.57	1.47
HD 151804	2	5.95	3.0± 2.3	148± 15	5.0	–	1.3	V	M	B17	1.1 ± 0.1	43 ± 0.8	-8 ± 1.6	1.12	0.57	1.21
HD 152235	1	17.9	2.1± 2.4	138± 67	15	–	2.2	V	M	B17	0.8 ± 0.1	115 ± 1.5	-6 ± 2.7	0.79	0.47	1.54
HD 152245	2	6.15	0.7± 2.4	142± 3	5.1	–	1.1	V	M	2015-02-06	0.9 ± 0.1	49 ± 1.1	-7 ± 1.7	0.93	0.62	1.48
HD 152249	1	15.9	2.2± 2.4	144± 10	13	2.5	1.6	G	S	B17	0.3 ± 0.1	64 ± 3.9	-27 ± 6.2	0.30	0.65	2.37
HD 153919	2	5.28	1.4± 2.3	80± 20	4.4	–	2.0	V	M	B17	2.7 ± 0.1	10 ± 0.3	7 ± 1.2	2.67	0.57	1.09
HD 154445	23	1.27	16.6± 2.1	180± 1	1.1	–	1.2	F	S	2020-10-03	3.7 ± 0.1	91 ± 0.2	3 ± 0.6	3.74	0.56	1.15
HD 156247	22	0.78	15.1± 2.1	178± 1	0.7	–	0.7	F	S	2020-10-03	2.0 ± 0.1	87 ± 0.2	2 ± 0.5	2.04	0.56	1.20
HD 162978	0	40.7	2.1± 2.4	126± 36	34	–	1.2	V	M	2018-11-06	1.3 ± 0.1	-1 ± 0.3	3 ± 0.8	1.41	0.65	1.53
HD 163181	4	3.71	2.6± 2.4	75± 10	3.1	–	2.4	V	M	B17	1.4 ± 0.1	175 ± 1.2	19 ± 3.0	1.44	0.47	0.38
HD 164073	13	0.80	8.5± 2.1	97± 5	0.7	–	1.1	F	S	B17	1.1 ± 0.1	1 ± 0.7	-3 ± 1.2	1.10	0.63	1.11
HD 164402	0	57.5	2.4± 2.2	113± 19	48	–	0.7	V	S	2020-10-03	0.2 ± 0.1	4 ± 2.8	-8 ± 3.8	0.22	0.52	2.10
HD 164536	1	31.8	2.1± 2.2	106± 38	26	–	0.9	F	S	2020-10-03	0.8 ± 0.1	159 ± 0.7	-7 ± 1.2	0.79	0.55	1.28
HD 164816	1	36.7	1.3± 2.1	98± 43	31	–	1.0	G	S	2019-02-27	0.1 ± 0.1	51 ± 3.7	61 ± 42.3	0.11	0.44	2.50

Notes. The columns are explained in Sect. 2. B17 refers to Bagnulo et al. (2017), and S14 to Siebenmorgen et al. (2014).

Table A.1. continued.

1	2	3	4	5	6	7	8	9	10	11	12	13	14	15	16	17
Star		*Planck*				Reddening				FORS				Serkowski		
Name	$\|\|b\|\|$	I_{850} MJy/sr	p_{850} %	θ_{850} °	A_V^{850} mag	A_V mag	$A_V^{\rm ref}$ mag	Ref	SM	Date	p_V %	θ_V °	$\mathrm{d}\theta/\mathrm{d}\lambda$ °/µm	$p_{\rm max}$ %	$\lambda_{\rm max}$ µm	$k_{\rm pol}$
HD 164906	1	36.2	1.3± 2.1	109± 14	30	–	2.2	G	S	2020-10-03	0.2 ± 0.1	5 ± 4.5	19 ± 8.2	0.24	0.80	2.50
HD 164947A	1	23.9	1.4± 2.2	111± 51	20	–	1.1	F	S	2020-10-03	0.5 ± 0.1	72 ± 1.2	17 ± 2.8	0.53	0.56	0.88
HD 164947B	1	23.8	1.4± 2.2	111± 28	20	–	1.1	F	S	2020-10-03	0.6 ± 0.1	49 ± 1.0	-5 ± 1.8	0.59	0.60	0.90
HD 167264	2	9.02	1.7± 2.2	151± 41	7.5	–	1.0	V	S	2020-10-03	0.5 ± 0.1	102 ± 1.3	11 ± 2.1	0.57	0.65	1.80
HD 167771	1	13.2	1.2± 2.3	59± 78	11	2.2	1.5	G	S	2019-02-20	0.5 ± 0.1	47 ± 0.9	16 ± 2.6	0.57	0.68	1.24
”										2019-03-19						
HD 167838	0	24.7	2.3± 2.1	122± 66	21	–	2.1	V	M	B17	0.3 ± 0.1	97 ± 2.7	48 ± 8.7	0.32	0.57	1.56
HD 168076	1	40.5	2.4± 2.2	146± 11	34	–	2.6	V	M	B17	3.4 ± 0.1	66 ± 0.3	-5 ± 0.9	3.41	0.58	1.33
HD 168941	6	1.47	0.8± 2.3	80± 60	1.2	–	1.2	G	M	2019-03-03	0.1 ± 0.1	50 ± 3.9	-18 ± 4.2	0.15	0.73	1.35
HD 169454	1	36.6	2.4± 2.2	119± 14	30	–	3.6	V	S	B17	2.1 ± 0.1	15 ± 0.8	-9 ± 1.6	2.12	0.58	1.26
HD 170740	1	25.9	2.2± 2.1	129± 38	22	–	1.4	F	M	B17	2.0 ± 0.1	77 ± 0.5	-5 ± 0.9	1.98	0.56	1.23
HD 175156	8	1.33	1.8± 2.4	80± 52	1.1	–	1.1	V	S	2020-10-03	0.5 ± 0.1	42 ± 1.1	18 ± 3.7	0.54	0.54	1.23
HD 180968	5	2.98	2.3± 1.7	30± 84	2.5	–	0.8	F	S	2019-04-08	0.5 ± 0.1	36 ± 0.7	-1 ± 0.9	0.52	0.53	1.05
HD 185418	2	4.03	2.7± 1.9	148± 34	3.4	–	1.4	G	M	2019-03-25	0.8 ± 0.1	24 ± 0.4	-1 ± 1.2	0.84	0.60	1.65
HD 185859	1	7.09	4.3± 1.8	111± 16	5.9	–	1.6	V	S	2020-10-04	2.2 ± 0.1	5 ± 0.2	-4 ± 0.7	2.27	0.50	1.25
”										2020-10-06						
HD 203532	32	1.14	7.4± 1.7	48± 12	1.0	–	0.9	F	S	2018-11-05	1.4 ± 0.1	126 ± 0.4	-1 ± 0.6	1.41	0.58	1.21
HD 210121	44	0.85	8.8± 2.0	46± 20	0.7	–	0.8	F	S	B17	1.3 ± 0.1	156 ± 1.1	9 ± 1.7	1.35	0.44	0.48
HD 287150	21	1.23	8.5± 2.7	172± 11	1.1	1.1	1.2	F	S	2019-03-19	1.5 ± 0.1	72 ± 0.3	0 ± 0.4	1.51	0.56	0.97
HD 294264	19	19.9	3.0± 2.0	13± 26	17	–	2.8	F	M	2019-03-18	2.8 ± 0.1	78 ± 0.3	3 ± 0.5	3.14	0.72	1.37
”										2019-03-19						
HD 294304	17	2.16	1.8± 2.0	68± 18	1.8	1.6	1.2	F	S	2020-10-01	0.7 ± 0.1	140 ± 1.5	-18 ± 2.8	0.70	0.52	1.47
HD 303308	1	44.0	0.6± 1.4	148± 41	37	–	1.4	V	M	B17	2.9 ± 0.1	99 ± 0.2	0 ± 0.4	2.92	0.55	1.32
HD 315021	1	25.6	1.4± 2.1	110± 36	21	1.7	1.2	F	S	2019-02-10	0.4 ± 0.1	56 ± 2.3	11 ± 2.4	0.44	0.62	1.38
HD 315023	1	25.0	0.9± 2.0	122± 61	21	1.8	1.5	F	S	B17	1.3 ± 0.1	151 ± 0.7	1 ± 0.9	1.40	0.68	1.41
HD 315024	1	28.3	1.4± 2.1	109± 16	24	2.1	1.2	F	S	2020-10-04	0.1 ± 0.1	183 ± 9.2	-130 ± 29.3	0.10	0.43	2.50
HD 315031	1	32.3	1.4± 2.1	109± 26	27	–	1.2	F	S	2020-10-04	0.6 ± 0.1	45 ± 0.8	-9 ± 1.8	0.58	0.64	0.95
HD 315032	1	41.7	1.4± 2.1	109± 48	35	1.6	1.0	F	S	2020-10-04	0.2 ± 0.1	66 ± 3.8	29 ± 5.5	0.19	0.87	0.50
HD 315033	1	41.0	1.0± 2.1	102± 83	34	–	1.4	V	S	2020-10-04	0.4 ± 0.1	95 ± 1.5	17 ± 3.1	0.41	0.64	1.65
Herschel 36	1	58.9	1.1± 2.3	91± 87	49	–	0.7	F	S	2020-10-05	6.8 ± 0.2	95 ± 0.2	3 ± 0.5	7.19	0.64	1.61
Walker 67	1	58.9	1.1± 2.3	91± 16	49	–	0.7	F	S	B17	4.1 ± 0.3	17 ± 0.6	-6 ± 1.2	5.17	0.81	1.47